A&A 476, 759–777 (2007)
DOI: 10.1051/0004-6361:20042439

Astronomy & Astrophysics

The soft X-ray properties of AGN from the CJF sample

A correlation analysis between soft X-ray and VLBI properties⋆

S. Britzen[1,2,3], W. Brinkmann[4], R. M. Campbell[5], M. Gliozzi[4,6], A. C. S. Readhead[7], I. W. A. Browne[8], and P. Wilkinson[8]

[1] Max-Planck-Institut für Radioastronomie, Auf dem Hügel 69, 53121 Bonn, Germany
e-mail: sbritzen@mpifr-bonn.mpg.de
[2] Landessternwarte, Königstuhl, 69117 Heidelberg, Germany
[3] ASTRON, Oude Hoogeveensedijk 4, 7991 PD Dwingeloo, The Netherlands
[4] Max-Planck-Institut für extraterrestrische Physik, Giessenbachstrasse 1, 85748 Garching, Germany
[5] Joint Institute for VLBI in Europe, Oude Hoogeveensedijk 4, 7991 PD Dwingeloo, The Netherlands
[6] Department of Physics and Astronomy, George Mason University, 4400 University Drive, MS 3F3, Fairfax, VA 22030, USA
[7] California Institute of Technology, Department of Astronomy, 105-24, Pasadena, CA 91125, USA
[8] University of Manchester, Nuffield Radio Astronomy Laboratories, Jodrell Bank, Macclesfield, Cheshire SK11 9 DL, UK

Received 26 November 2004 / Accepted 2 October 2007

ABSTRACT

Context. We present the soft X-ray properties obtained in the ROSAT All-Sky survey and from pointed PSPC observations for the AGN in the complete flux-density limited Caltech-Jodrell Bank flat spectrum sample (hereafter CJF). CJF is a VLBI survey (VLBA observations at 5 GHz) of 293 AGN with detailed information on jet component motion.
Aims. We investigate and discuss the soft X-ray properties of this AGN sample and examine the correlations between X-ray and VLBI properties, test beaming scenarios, and search for the discriminating properties between the sub-samples detected and not detected by ROSAT.
Methods. Comparing the observed and the predicted X-ray fluxes by assuming an Inverse Compton (IC) origin for the observed X-rays, we compute the beaming or Doppler factor, $\delta_{\rm IC}$, for the CJF sources and compare it with the equipartition Doppler factor, $\delta_{\rm EQ}$. We further contrast the Doppler factors with other beaming indicators derived from the VLBI observations, such as the value of the expansion velocity, and the observed and intrinsic brightness temperature. We calculate two different core dominance parameters (R): the ratio of total VLBI flux to single-dish flux, $R_{\rm V}$, and the ratio of the VLBI core-component flux to single-dish flux, $R_{\rm C}$. In addition, we investigate the large-scale radio structure of the AGN and the difference between the pc- and kpc-scale structure (misalignment) with regard to the X-ray observations.
Results. We find a nearly linear relation between X-ray and radio luminosities, and a similar but less stringent behaviour for the relation between optical and X-ray luminosities. The CJF-quasars show faster apparent motions and larger values of $\delta_{\rm IC}$ than the radio galaxies do. The quasars detected by ROSAT have a different $\beta_{\rm app}$-redshift relationship compared to the non-detected ones. We find no significant difference in R between the quasars detected and not detected by ROSAT. We find evidence that R is larger for quasars and BL Lac objects than it is for radio galaxies, in accordance with unification scenarios. ROSAT-detected sources tend to reveal extended large-scale radio structures more often.
Conclusions. We conclude that beaming alone cannot explain the observed dichotomy of ROSAT detection or non-detection and assume that the large-scale jet structure plays a decisive role.

Key words. instrumentation: interferometers – galaxies: active – X-rays: galaxies – radio continuum: galaxies

1. Introduction

The investigation of the origin and nature of radiation processes in AGN requires the combination of multifrequency flux-density observations and morphological information to pinpoint the emission regions. Only recently have *CHANDRA* observations been able to clarify the dominant X-ray emission mechanism for a number of individual sources. 78 radio galaxies, quasars, and BL Lac objects with known X-ray emission from jets or hotspots are now known (http://hea-www.harvard.edu/XJET/). The nature of the X-ray emission processes in most of the remaining AGN is a matter of debate and a statistical treatment of this phenomenon for a larger sample of AGN is still lacking.

The CJF survey has recently provided a kinematic database suited for an improved statistical treatment of such questions related to AGN. All CJF sources have been monitored in at least three epochs at 5 GHz with the VLBA. Detailed information concerning the observations, the data reduction, and the source parameters resulting from the model-fitting procedure can be found in Britzen et al. (2007a, hereafter Paper I). The kinematic analysis of the sources is described in Britzen et al. (2007b, hereafter Paper II). Most (57%) of these sources have been detected in the *ROSAT* All-Sky Survey. Although we lack simultaneous observations when comparing the radio and the *ROSAT* data, we do have the possibility to check the basic concepts of beaming with this largest uniform sample so far.

The discovery of well-collimated, one-sided, apparently superluminal jets on parsec scales by VLBI has revealed the

⋆ Tables 3–6 are only available in electronic form at http://www.aanda.org

dominant effects of relativistic beaming on the appearance of these objects (e.g., Witzel et al. 1988; Readhead 1993; Zensus & Pearson 1987), and has motivated the development of the so-called "unified theories" for quasars and radio galaxies (Orr & Browne 1982; Barthel 1989; Urry & Padovani 1995). The viewing angles are expected to differ among the source classes, with quasars and BL Lacertae objects being radio galaxies seen with their jets forming a small angle with respect to the line of sight. The observed superluminal motions strictly require that some "phase" or "pattern" speed of a wave traveling along the jet is relativistic, but there are strong arguments also for the bulk velocity of the radiating plasma to be relativistic, with associated forward beaming of the emitted radiation (e.g., Witzel et al. 1988; Eckart et al. 1989). The comparison of Doppler factors calculated on the basis of velocity and X-ray information may answer the question whether the pattern and the bulk velocities are different.

Since part of the X-ray emission is isotropic and part is beamed Inverse Compton radiation from the radio jet, we can place limits on the IC Doppler factor $\delta_{\rm IC}$. The Doppler factors can be derived via the standard synchrotron self-Compton (SSC) argument, from equipartition arguments ($\delta_{\rm EQ}$), and from the apparent velocities determined from VLBI observations.

Most models, accounting for the observed broadband spectra of blazars, attribute the radio through optical emission to synchrotron radiation, and X-ray through γ-ray emission to Compton scattering (e.g., Marscher 1980; Königl 1981). The models differ in the location and structure of the acceleration and emission region(s). However, in the case of the so-called High Peaked BL Lac objects (HBL), even the X-ray emission is thought to be due to synchrotron radiation (e.g., Padovani & Giommi 1995). The X-ray emission from knots in radio jets can mainly be attributed to synchrotron emission. Convincing evidence for this has been found in the optical polarization of M87, suggesting that the optical emission as well as the radio emission are produced via the synchrotron process (Harris et al. 1998; Biretta et al. 1991). On the other hand, X-ray intensities that lie well above the extrapolation of the radio/optical synchrotron spectrum are taken to be strong evidence against the "simple" synchrotron model. In addition, every synchrotron source must also produce IC emission from at least the CMB and the synchrotron photons themselves.

In this paper we combine and correlate information from different parts of the electromagnetic spectrum, i.e. the radio and the X-ray regime. We test the beaming and unification scenario on the basis of data obtained in the CJF survey and the *ROSAT* All-Sky Survey (RASS).

The RASS was the first soft X-ray survey of the whole sky using an imaging telescope (Trümper 1983). It was performed from August 1, 1990 to February 1, 1991 and yielded ~125 000 X-ray sources with a positional accuracy such that 68% of the sources are found within 20″ from their corresponding optical counterparts (Voges et al. 2000) and a limiting sensitivity of a few times 10^{-13} erg/cm^2/s in the 0.1−2.4 keV energy band, depending on the spectral form and the amount of galactic absorption. The survey was followed by a period of pointed observations lasting until February 12, 1999; the PSPC (Position Sensitive Proportional Counter) detector (Pfeffermann et al. 1986) exhausted its gas supply earlier, in September 1994.

This paper is organized as follows: Sects. 2 and 3 introduce the CJF data and the *ROSAT* X-ray data respectively; Sect. 4 presents the results of the correlation analysis with regard to the X-ray properties of the CJF survey, the $\beta_{\rm app}$-relation, the IC Doppler factor, the equipartition Doppler factor, the brightness temperature, the core dominance parameter, the misalignment, and the relation between the large scale structure of AGN and the observed X-ray emission. Finally, Sect. 5 briefly discusses our results.

2. The CJF data

The CJF, defined by Taylor et al. (1996), is a complete flux-limited sample of 293 flat-spectrum radio sources, drawn from the 6 cm and 20 cm Green Bank Surveys (Gregory & Condon 1991; White & Becker 1992) with selection criteria as follows: $S\,(6\ {\rm cm}) \geq 350$ mJy, $\alpha^6_{20} \geq -0.5$, $\delta(1950) \geq 35^\circ$, and $|b^{\rm II}| \geq 10^\circ$. This sample is mostly a superset of the flat-spectrum sources in the Pearson-Readhead Survey (Pearson & Readhead 1988) based on the 6 cm MPI-NRAO 5 GHz surveys (Kühr et al. 1981), the First Caltech-Jodrell Bank Survey (CJ1: Polatidis et al. 1995; Thakkar et al. 1995; Xu et al. 1995) and the Second Caltech-Jodrell Bank Survey (CJ2: Taylor et al. 1994; Henstock et al. 1995). Continued VLBI observations of the CJF sources have been performed since 1990. For the unambiguous determination of the jet component position and motion parameters at least three observing epochs (spread over roughly 4 years) have been obtained for all of the 293 objects. All epochs for all sources have been analyzed in the same systematic way in order to create a homogeneous, statistically valid database. A reanalysis of "early" epochs has been done in parallel with the acquisition and analysis of new observational epochs, which led to a simultaneous completion of the observation, reduction, and reanalysis parts. For details on the observations and data reduction see Paper I.

The redshifts of the identified quasars in CJF range from $z = 0.227$ to $z = 3.889$, with an average of 16 quasars per redshift interval of 0.2 in the range $z = 0.6$−2.6. This provides us with the opportunity to investigate possible correlations over a broad range of redshifts and to address important cosmological questions, such as AGN evolution with cosmic epoch. The CJF is now known to contain some 25 radio galaxies and 11 BL Lac objects at $z > 0.6$, enough to allow a meaningful comparison of the properties of these source classes at the same redshift and luminosity.

Preliminary results have already been discussed in Britzen et al. (2001) and Britzen (2002). The kinematics of the complete sample is investigated and discussed in detail in Paper II.

The results presented here are based on a careful identification of the jet components across the epochs and multiple checks of the resulting motions in the xy-plane (see Papers I and II). It turned out that not all jet components can yield proper motion estimates of equal significance. We assigned a quality factor to each component that takes the following properties of each jet component into account:

- the jet component has to be clearly separated from other components and the core;
- the component should be unambiguously identifiable in each epoch in which it is detected (i.e., it should not appear to merge with other components nor appear to split into two components at any epoch);
- the component should be visible in at least three epochs.

Single, bright jet components that are clearly separate in all epochs were given a quality 1, while all components that merge or split were assigned a quality 3. With these additional quality criteria, we can additionally select only the most reliable jet

component proper motions for further consideration. For a detailed discussion of these quality factors please see Paper II. For source-based comparisons in this paper, e.g., between $\beta_{\rm app}$ and $\delta_{\rm IC}$, we use a "representative" subsample of jet components. In several tests we determined these jet components to be representative for jet component motion in this source. The so-called "brightest" subsample – described in detail in Paper II – fulfills these criteria and will be used as comparison VLBI-sample for the correlation analysis between *ROSAT* – and VLBI-information presented in this paper. Wherever possible, e.g., the calculation of the core dominance parameter R or the misalignment, the complete sample of CJF sources has been used.

3. The *ROSAT* X-ray data

For each of the sample sources a $1^\circ \times 1^\circ$ field centered on the radio position was extracted from the RASS and analyzed using a procedure based on standard routines within the EXSAS environment (Zimmermann et al. 1994). This procedure uses a maximum-likelihood source detection algorithm (Cruddace et al. 1988), which returns the likelihood of the existence of an X-ray source at the specified radio position, the number of source photons within 5 times the FWHM of the PSPC's point spread function, and the error in the number of source photons (Cruddace et al. 1988). For the RASS, the FWHM of the PSPC point spread function is estimated to be ∼60 arcsec (Zimmermann et al. 1994). Since it is known that an AGN is present at the position of the radio source, we considered a radio source to be detected in X-rays if the likelihood of existence is greater than 5.91, which corresponds to 3σ. If no X-ray source is detected above the specified significance level, we determined the 2σ upper limit on the number of X-ray photons. To calculate the corresponding count rates we used the vignetting-corrected RASS exposure averaged over a circle with radius 5 arcmin centered on the radio position.

Several of the sources, mostly well-studied radio sources of the CJF, had been targets of pointed observations. We extracted the data for these from the *ROSAT* archive and used them in the following analysis, as they are in general of superior statistical significance. In particular, if a source is not detected in the survey but is a target of a pointed observation or found serendipitously in a pointed observation, we used the pointed data in the analysis.

The unabsorbed X-ray fluxes are calculated from the measured count rates by assuming power laws for the X-ray spectra with average photon indices of $\Gamma = 1.8$ for radio galaxies, $\Gamma = 2.2$ for quasars, and $\Gamma = 2.1$ for all other objects and Galactic absorption (Dickey & Lockman 1990; Stark et al. 1992; for details see Brinkmann et al. 1994). For correlations with the recent radio data we used for the luminosity determination a cosmology with $h = 0.71$, $\Omega_{\rm m}h^2 = 0.135$, and $\Omega_{\rm tot} = 1.02$ (for details see Sect. 4.2.7). It should be noted that a slightly incorrect value of the power law slope does not influence the flux determination dramatically; the main source of uncertainty is the amount of absorption of the soft X-rays. The stated errors merely reflect the errors in the counting statistics of the survey sources and do not incorporate deviations from the assumed power law slope, additional absorption, or other systematic errors. Therefore, for weaker sources a total error of the X-ray flux of the order of $\lesssim$25% must be regarded as a conservative estimate.

4. Results

In Table 1 we present the relevant data for all 293 sources. Columns 1 and 2 give the IAU designation of the radio source, followed by a common name of the object, if available, and the JVAS J2000 name (Wilkinson et al. 1998; Browne 1998). In case the source is not observed within JVAS, we used the Véron-Cetty & Véron (2001) edition of *A Catalogue of Quasars and Active Nuclei*, or the CLASS source name (Myers et al. 2003). Column 3 lists the type of the object: Quasars (Q), BL Lac objects (B), radio galaxies (G), High Polarized Quasars (HPQ), Low Polarized Quasars (LPQ), Compact Symmetric Objects (CSO), Seyfert galaxies type 1 (Sy 1), Seyfert galaxies type 2 (Sy 2), sources with peculiar properties (pec) or sources belonging to a cluster of objects (cluster). The next three columns give the redshift, its optical magnitude (mostly obtained from NED) and the 5 GHz Green Bank flux. It should be noted that in several cases different data exist for one source, mainly for the type and the magnitude, and we were not always able to resolve the discrepancies. The next column (7, EXML) gives the likelihood of the existence of an X-ray source at the radio position in the RASS, as described in Sect. 3, followed in Col. (8) by the 0.1−2.4 keV X-ray flux density with its statistical error in units of 10^{-12} erg cm^{-2} s^{-1}. If the source is not detected at a 3σ level and no pointed observations are available, we give the 2σ upper limit to the flux density and no uncertainty in Col. (8). We further want to caution that for a couple of sources the given X-ray flux may not originate exclusively from the radio/optical object: there are sources with another prominent object nearby (which is not the radio source) or which reside in a cluster of radio galaxies (like NGC 1275) where the X-ray emission must be primarily attributed to the cluster.

Column 9 indicates whether a source has been found by the standard analysis of the *ROSAT* Survey data ("s"), and thus the data have been published already elsewhere, or whether it was found in the field of a pointed PSPC or HRI observation ("p").

Further radio data follow in Cols. 10 to 13. Column 10 introduces a system of comments to describe the VLA structure of the sources. In addition, references for the VLA maps are given. The abbreviations are explained explicitly in Table 2. In addition, this column lists in boldface a value describing jet structure on large (VLA) scales in order to quantify the complexity of the extended emission. This is the complexity-factor (see Sect. 4.3.2 for a more detailed description). Its maximum value is 5, describing the most complex extended structure.

Some individual sources merit comment before we proceed. We searched ADS and NED for large-scale information on the sources. For the following sources no VLA map could be found in the literature: 0344+405, 0615+820, 0800+618, 1305+804, 1306+360, 1818+356, 2116+818. The X-ray/radio source 0450+844 appears to be associated with a background/foreground galaxy and can be understood as the active nucleus of a galaxy (17−18 mag) possibly dominating a cluster; there are several faint objects in the vicinity of the optical galaxy on the POSS plate (Johnston et al. 1984). The same seems to be true for the source 1010+350: it is point-like in VLA observations, and its X-ray emission seems to come from a surrounding cluster.

We wish to mention that the information on the extended structure has been collected from the literature (cited in Table 2) and due to the different map qualities results in an inhomogeneous data base. Point-like structures seen in these maps do not necessarily imply that these sources have no large-scale structure; any such putative large-scale structure may fall below the

Table 1. CJF sources in the *ROSAT* All Sky Survey.

CJF name		type	z	m_v	S_m [mJy]	EXML	$f_x \times 10^{-12}$ [erg/cm^2/s]	OBS	VLA structure	$\theta_{\rm VLA}$ [deg]	$\theta_{\rm VLBI}$ [deg]	ΔPA [deg]
(1)	(2)	(3)	(4)	(5)	(6)	(7)	(8)	(9)	(10)	(11)	(12)	(13)
0003+380	S4 0003+38, JVAS J0005+3820	G,Sy	0.229	19.4	549	5.83	0.49		R[1,4], **1**	110	120	10
0010+405	4C +40.01, JVAS J0013+4051	G	0.255	17.9	1040	34.60	1.61 ± 0.38	s	R[27], **1**	335	330	5
0014+813	S5 0014+81, JVAS J0017+8135	Q	3.366	16.5	551	43.03	2.40 ± 0.47	ps	U[1], **0**	/	189	/
0016+731	S5 0016+73, JVAS J0019+7327	Q	1.781	18.0	1712	4.45	0.58	p	J[1], **2**	4	170	166
0018+729	S5 0018+72, JVAS J0021+7312	G		22.4	397	0.79	0.11		U[1], **0**	/	277	/
0022+390	B3 0022+390, JVAS J0025+3919	Q	1.946	19.8	663	4.14	0.39		J[1], **2**	21	164	143
0035+367	4C +36.01, [VCV2001] J003746.2+365911	Q	0.366	18.0	482	8.40	0.50 ± 0.21	s	J[27], **3**	13	357	16
0035+413	S4 0035+41, JVAS J0038+4137	Q	1.353	19.9	1114	10.36	0.77 ± 0.29	s	J[1] **1**	115	106	9
0102+480	JVAS J0105+4819				1088	2.89	0.33		U[1], **0**	/	47	/
0108+388	OC +314, JVAS J0111+3906	G	0.669	22.0	1321	1.14	0.21		J[5] **2**	90	249	159
0109+351	B2 0109+35, JVAS J0112+3522	Q	0.45	17.8	362	19.03	1.23 ± 0.33	s	JCJ[1], **4**	40/278	205	73
0110+495	S4 0110+49, JVAS J0113+4948	Q	0.389	18.4	710	31.87	2.31 ± 0.58	s	?[27], **?**	55	329	86
0133+476	DA 55, JVAS J0136+4751	HPQ	0.859	18.	1816	2.04	0.75	p	U[1], **0**	/	328	/
0145+386	JVAS J0148+3854	Q	1.442	16.	370	1.05	0.12		U[1], **0**	/	311	/
0151+474	B3 0151+474, JVAS J0154+4743	Q	1.026	20.5?	505	2.22	0.17		U[1], **0**	/	184	/
0153+744	S5 0153+74, JVAS J0157+7442	Q	2.338	16.0	1549	12.82	0.95 ± 0.34	ps	U[1,15,25], **0**	/	~160	/
0205+722	S5 0205+72, [VCV2001] J020952.2+722924	G	0.895	20.7	560	2.45	0.47		U[1], **0**	/	252	/
0212+735	S5 0212+73, JVAS J0217+7349	HPQ	2.367	19.	2278	30.11	2.45 ± 0.58	ps	R[1], **1**	147	103	44
0218+357	S4 0218+35, JVAS J0221+3556	G_L	0.936	20.0	1498	3.30	0.26		JCJ[14,27], **3**	70	/	/
0219+428	3C 066A, [VCV2001] J022239.6+430208	B	0.444	15.5	806	11.63	5.28 ± 1.86	s	J[2], **2**	168	176	8
0227+403	B3 0227+403, JVAS J0230+4032	Q	1.019	17.0	436	0.40	0.35		U[1], **0**	/	142	/
0248+430	B3 0248+430, JVAS J0251+4315	LPQ	1.310	17.45	1414	14.37	1.31 ± 0.41	s	cJ[1], **3**	107	143	36
0249+383	B3 0249+383, JVAS J0253+3835	Q	1.122	18.5	450	1.19	0.25		R[1], **1**	/	341	/
0251+393	B3 0251+393, JVAS J0254+3931	Q	0.289	17.0	408	65.39	3.28 ± 0.57	s	J[1], **2**	102	86	16
0256+424	B3 0256+424, JVAS J0259+4235	Q	0.867	19.5?	366	3.12	0.42		R[1], **1**	280	/	/
0307+380	B3 0307+380, JVAS J0310+3814	Q	0.816	20.0?	760	2.54	0.39		U[1], **0**	/	48	/
0309+411	S4 0309+41, JVAS J0313+4120	Q,Sy1	0.134	18.0	516	>100	5.47 ± 0.64	ps	J[1], **2**	310	307	3
0316+413	NGC 1275, JVAS J0319+4130	G/C	0.018	12.64	42370	>100	283.9 ± 5.97	ps	JCJ,H[12,13], **5**	160(235)	180	20
0340+362	JVAS J0343+3622	Q	1.485	20.0[r]	376	3.01	0.66	s	JCJ[1], **3**	50	31	19
0344+405	4C +40.12,	G	0.039	16.5	478	3.83	0.75		/	/	/	/
0346+800	S5 0346+80, JVAS J0354+8009	Q[r]		21.3	396	0.91	0.09		U[1], **0**	/	~130	/
0402+379	B3 0402+379, JVAS J0405+3803	G,Sy	0.055	17.2	937	91.29	5.70 ± 0.82	s	JCJ,H[1,27], **5**	223/~22	~250/34	27/12
0424+670	JVAS J0429+6710	Q	0.324	21.0?	362	1.37	0.20		R[27], **1**	280	/	/
0444+634	S4 0444+63, JVAS J0449+6332	Q	0.781	19.7	606	3.73	0.79	s	R[1], **1**	176	174	2
0454+844	S5 0454+844, JVAS J0508+8432	B	0.112	16.5	1398	26.14	1.03 ± 0.27	ps	U[1], **0**	/	161	/
0537+531	S4 0537+53, JVAS J0541+5312	Q	1.275	18.0	665	0.26	0.41 ± 0.09	p	JCJ[1], **3**	34	318	76
0546+726	S5 0546+72, [VCV2001] J055253.0+724045	Q,C.g.l.	1.555	17.0	401	8.56	0.84 ± 0.37	s	J[1], **2**	150	300	150
0554+580	JVAS J0559+5804	Q	0.904	18.0	906	0.70	0.25		J[1], **2**	328	285	43
0600+442	B3 0600+442, JVAS J0604+4413	G[r]	1.136	21.5?[r]	705	24.67	1.66 ± 0.46		U[1,27], **0**	/	316	/
0602+673	S4 0602+67, JVAS J0607+6720	Q	1.95	20.6	657	9.24	0.99 ± 0.39	s	U[1,27], **0**	/	172	/
0604+728	4C +72.10, JVAS J0610+7248	Q	0.986	20.3	654	4.90	0.63	s	JCJ[1], **3**	72/286	105/270	33/16
0609+607	JVAS J0614+6046	Q	2.702	19.0	1059	7.0	0.38 ± 0.20	s	U[1], **0**	/	152	/
0620+389	B3 0620+389, JVAS J0624+3856	Q,cluster?	3.469	20.0	811	7.02	1.06 ± 0.49	s	R[1,27], **1**	0	138	138
0621+446	JVAS J0625+4440	B		18.0	369	7.59	1.03 ± 0.46		U[27], **0**	/	/	/
0615+820	S5 0615+82, JVAS J0626+8202	LPQ	0.710	17.5	999	2.45	0.23	p	/	/	/	/
0627+532	JVAS J0631+5311	Q	2.204	18.5	485	3.77	0.57		U[1], **0**	/	~50	/
0633+596	JVAS J0638+5933				482	1.61	0.23		U[1], **0**	/	241	/
0633+734	S5 0633+73, JVAS J0639+7324	Q	1.85	17.8	748	9.96	0.57 ± 0.26		J[1], **2**	321	353	32
0636+680	S4 0636+68, JVAS J0642+6758	Q	3.174	16.46	499	0.31	0.14	p	U[1], **0**	/	/	/
0641+393	B3 0641+391, JVAS J0644+3914	Q	1.266	19.5	453	0.48	0.19		J[1], **2**	67	4	63
0642+449	S4 0642+44, JVAS J0646+4451	LPQ	3.396	18.49	1191	2.31	0.39	p	U[1], **0**	/	90	/
0646+600	S4 0646+60, JVAS J0650+6001	HPQ	0.455	18.9	920	1.29	0.22		U[1], **0**	/	216	/
0650+371	S4 0650+37, JVAS J0653+3705	Q	1.982	18.0	977	4.02	0.62		U[1], **0**	/	56	/
0650+453	B3 0650+45, JVAS J0654+4514	Q	0.933	21.0	420	2.07	0.28	s	R[1], **1**	332	85	113
0651+410	CGCG 204-027, JVAS J0655+4100	G	0.022	14.6	425	3.29	0.34		U[1], **0**	/	156	/
0700+470	B3 0700+470, JVAS J0704+4700	G[r]		20[r]	443	1.83	0.28		U[1], **0**	/	~90	/
0702+612	JVAS J0707+6110	Q[r]		17.0	370	4.59	0.24		J[1,27], **2**	~70	70	0
0707+476	B3 0707+476, JVAS J0710+4732	LPQ	1.292	18.2	906	0.00	0.00		JCJ[3], **4**	279/99	~25	74
0710+439	S4 0710+43, JVAS J0713+4349	G[r]	0.518	19.7	1629	1.03	0.59 ± 0.06	**p**	R[1], **1**	~170	180	10
0711+356	S4 0711+35, JVAS J0714+3534	LPQ	1.620	17.	901	5.04	0.33	ps	JCJ[3], **3**	145	157	12
0714+457	S4 0714+457, JVAS J0717+4538	Q	0.940	19.0	480	2.24	0.32		U[1], **0**	/	132	/
0716+714	S5 0716+714, JVAS J0721+7120	B		15.5	788	>100	4.31 ± 0.51	ps	J,H[11], **5**	300	15	75
0718+793	JVAS J0726+7911				631	2.58	0.18	s	U[1], **0**	/	296	/
0724+571	JVAS J0728+5701	Q	0.426	17.0	393	1.80	0.27		U[1], **0**	/	152	/
0727+409	S4 0727+40, JVAS J0730+4049	Q,cluster?	2.500	19.3	468	15.09	1.10 ± 0.35	s	U[1,27], **0**	/	305	/
0730+504	TXS 0730+504, JVAS J0733+5022	Q	0.72	19.0	890	1.25	0.34		J[1], **2**	228	209	19
0731+479	S4 0731+47, JVAS J0735+4750	Q	0.782	18.	533	26.05	1.69 ± 0.44	s	U[1], **0**	/	270	/
0733+597	UGC 03927, JVAS J0737+5941	G	0.041	15.17	357	21.78	1.03 ± 0.29	s	U[1,27], **0**	/	~10	/
0738+491	JVAS J0742+4900	Q	2.32[r]	21.0?[r]	352	5.08	0.35		U[1], **0**	/	5	/
0740+768	JVAS J0747+7639	G[r]		19.5[r]	592	1.08	0.06		U[1], **0**	/	247	/
0743+744	S5 0743+74, JVAS J0749+7420	Q	1.629	19.3	479	5.93	0.28 ± 0.16	p	U[1,27], **0**	/	25	/
0746+483	S4 0746+48, JVAS J0750+4814	Q	1.951	18.5	860	6.94	0.51 ± 0.24	s	U[1,21], **0**	/	274	/
0749+540	4C +54.15, JVAS J0753+5352	B	>0.2	18.5	877	9.26	0.85 ± 0.30	s	U[1], **0**	/	~220	/
0749+426	B3 0749+426, JVAS J0753+4231	Q	3.59	18.1	461	2.03	0.26		U[1], **0**	/	220	/
0800+618	CLASS J0805+6144	Q[r]	3.044[r]	19.8[r]	981	4.02	0.42	s	/	/	152	/
0803+452	B3 0803+452, JVAS J0806+4504	Q	2.102	19.6	414	4.08	0.67		U[1], **0**	/	233	/
0804+499	S4 0804+49, JVAS J0808+4950	HPQ	1.432	17.5	1222	14.76	0.68 ± 0.24	ps	J[3], **2**	~200	145	55

Table 1. continued.

CJF name		type	z	m_v	S_m [mJy]	EXML	$f_x \times 10^{-12}$ [erg/cm^2/s]	OBS	VLA structure	$\theta_{\rm VLA}$ [deg]	$\theta_{\rm VLBI}$ [deg]	ΔPA [deg]
(1)	(2)	(3)	(4)	(5)	(6)	(7)	(8)	(9)	(10)	(11)	(12)	(13)
0805+410	B3 0805+410, JVAS J0808+4052	Q	1.420	19.0	743	27.83	1.15 ± 0.31	s	J[1], **2**	240	34	154
0806+573	TXS 0806+573, JVAS J0811+5714	Q	0.611	17.44	405	26.53	1.20 ± 0.30	s	J[1,27], **2**	~250	265	15
0812+367	B2 0812+36, JVAS J0815+3635	Q	1.025	18.0	980	7.0	0.30 ± 0.17	s	cJCJ[15,31], **5**	~350	349	1
0814+425	B3 0814+425, JVAS J0818+4222	B	0.245	18.5	1891	9.63	0.69 ± 0.33	ps	cJ[3], **3**	320	115	155
0820+560	S4 0820+56, JVAS J0824+5552	Q	1.409	18.0	1199	2.60	0.82 ± 0.09	p	J[16], **2**	309	82	133
0821+394	4C +39.23, CLASS J0824+3916	Q	1.216	18.5	1012	42.49	2.11 ± 0.44	s	J[1], **2**	139	318	179
0821+621	TXS 0821+621, JVAS J0825+6157	Q	0.542	17.6	615	41.02	1.90 ± 0.38	s	JCJ[1,29], **5**	47/236	244	8
0824+355	6C 0824+35, JVAS J0827+3525	Q	2.249	20.28	746	0.05	0.03		J[1], **2**	117	118	1
0831+557	4C +55.16, JVAS J0834+5534	G	0.240	19.0	5780	46.96	2.45 ± 0.53	s	JCJ[1,27], **4**	172/325	~305	20
0833+416	B3 0833+416, JVAS J0836+4125	Q	1.298	17.2	385	26.50	0.88 ± 0.24	s	JCJ[1], **3**	338/189	180	9
0833+585	S4 0833+58, JVAS J0837+5825	Q	2.101	18.0	669	8.53	0.54 ± 0.24	s	J[3], **3**	152	78	74
0836+710	4C +61.07, JVAS J0841+7053	Q	2.180	16.5	2423	>100	11.28 ± 0.82	ps	JCJ[3], **3**	204	211	7
0843+575	JVAS J0847+5723	G?[r]		23.0?[r]	384	0.25	0.09		U[1], **0**	/	42/~320	/
0847+379	4C +37.25, JVAS J0850+3747	G	0.407	19.5	382	8.45	0.36 ± 0.17	ps	JCJ,H[17], **5**	165	7	158
0850+581	4C +58.17, JVAS J0854+5757	Q	1.322	18.	1187	8.15	0.51 ± 0.22	ps	JCJ[18,19], **5**	139	156	17
0859+470	4C +47.29, JVAS J0903+4651	LPQ	1.462	18.7	1285	18.54	0.60 ± 0.18	s	D[3,16], **3**	330	352	22
0859+681	S4 0859+681, JVAS J0903+6757	Q	1.499	19.5	751	8.38	0.38 ± 0.17	s	U[27], **0**	/	14	/
0900+520	JVAS J0903+5151	Q	1.537	19.6	395	4.82	0.27		U[1], **0**	/	254	/
0902+490	S4 0902+49, JVAS J0905+4850	Q	2.690	18.5	547	10.24	0.54 ± 0.21		D[1], **3**	172	321	149
0917+449	B3 0917+449, JVAS J0920+4441	Q	2.18	19.0	1033	68.05	1.61 ± 0.26	s	JCJ[1], **4**	270/~170	190	20
0917+624	OK +630, JVAS J0921+6215	Q	1.446	19.5	1322	1.12	0.37 ± 0.02	p	J[3], **2**	238	343	105
0923+392	4C +39.25, JVAS J0927+3902	LPQ	0.699	17.86	7480	>100	3.56 ± 0.36	ps	JCJ[3], **3**	259	277	18
0925+504	RGB J0929+502, JVAS J0929+5013	B,cluster?		16.0	558	37.82	1.13 ± 0.23	s	U[1], **0**	/	128	/
0927+352	B2 0927+35, JVAS J0930+3503	B?[r]		19.2	383	28.88	0.79 ± 0.20	ps	J[30], **2**	280	285	5
0929+533	S4 0929+53, JVAS J0932+5306	Q	0.595	19.0	384	1.43	0.24		R[1], **1**	?	133	/
0930+493	TXS 0930+493, JVAS J0934+4908	Q	2.582	18.4	574	0.53	0.08		J[1], **2**	147	225	78
0942+468	B3 0942+468, JVAS J0945+4636	G	0.639[r]	20.61	354	3.40	0.16		U[1,27], **0**	/	41	/
0945+408	4C +40.24, JVAS J0948+4039	LPQ	1.252	17.5	1592	14.49	0.46 ± 0.16	s	D[3], **3**	32	116	84
0945+664	4C +66.09, CLASS J0949+6614	G	0.85?[r]	21.6	1407	0.00	0.00		D[27], **?**	35	/	/
0949+354	JVAS J0952+3512	Q	1.875	18	403	5.13	0.26		J[1], **2**	160	165	5
0950+748	S5 0950+748, JVAS J0954+7435	G	0.695[r]	21.7	738	0.83	0.05		U[1], **0**	/	253	/
0954+556	4C +55.17, JVAS J0957+5522	HPQ	0.909	17.7	2270	63.79	1.01 ± 0.17	ps	JCJ[3,16,23], **4**	~290/~45	195	95
0955+476	B3 0955+476, JVAS J0958+4725	Q	1.873	18.0	834	37.75	0.77 ± 0.16	ps	?[23], **?**	~120	127	7
0954+658	S4 0954+65, JVAS J0958+6533	B	0.368	16.7	1417	15.41	0.92 ± 0.29	ps	J[1,23], **2**	205	~290	85
1003+830	S5 1003+83, JVAS J1010+8250	G	0.322	20.5	716	29	0.92 ± 0.24		J[1], **2**	115	85	30
1010+350	B2 1010+35, JVAS J1013+3445	Q,cluster[#,$]	1.414	19.0	597	8.31	0.30 ± 0.14		U[1,27], **0**	/	96	/
1014+615	TXS 1013+615, JVAS J1017+6116	Q	2.80	18.12	631	7.68	0.21 ± 0.08		U[1,27], **0**	/	254	/
1015+359	S4 1015+35, JVAS J1018+3542	Q	1.226	18.09	587	14.80	0.57 ± 0.18	s	J[1], **2**	128	186	58
1020+400	4C +40.25, JVAS J1023+3948	Q	1.254	17.5	785	16.88	0.96 ± 0.28	ps	cD[1], **3**	22	318	64
1030+415	B3 1030+415, JVAS J1033+4116	HPQ	1.120	18.2	485	5.36	0.22		J[1], **3**	103/0	354	6
1030+398	B3 1030+398, JVAS J1033+3935	G[r]	1.095	21.5	645	2.87	0.12		U[1], **0**	/	~40	/
1030+611	S4 1030+61, JVAS J1033+6051	Q	0.336	19.7	579	13.77	0.21 ± 0.07		R[1], **1**	334	171	163
1031+567	S4 1031+56, JVAS J1035+5628	G, CSO	0.46	20.3	1200	1.71	0.08		U[1,27], **0**	/	220	/
1038+528	TXS 1038+528, JVAS J1041+5233	HPQ	0.677	17.4	709	64.41	1.06 ± 0.17	s	cJCJ[1,2], **5**	10,35,165	24	11
1041+536	7C 1041+5338, JVAS J1044+5322	Q	1.897	19.0	481	29.22	0.53 ± 0.13	s	U[1,27], **0**	/	~180	/
1039+811	S5 1039+81, JVAS J1044+8054	LPQ	1.254	16.5	1144	53.81	1.35 ± 0.24	ps	J[15,23], **2**	220	~280	60
1044+719	S5 1044+71, JVAS J1048+7143	Q	1.15	19.	2410	7.3	0.33 ± 0.02	s	cJ[1], **3**	219/337	107	112
1053+704	S5 1053+70, JVAS J1056+7011	Q	2.492	18.5	675	2.79	0.20		J[1], **2**	69	208	139
1053+815	S5 1053+81, JVAS J1058+8114	G	0.706	18.5	770	16.57	0.59 ± 0.19	ps	J[1], **2**	104	226	122
1058+726	4C +72.16, JVAS J1101+7225	Q	1.46	17.9	953	14.31	1.17 ± 0.34	ps	JCJ[1,27], **5**	222/335	5	30
1058+629	4C +62.15, JVAS J1101+6241	Q	0.663	17.7	700	70.04	0.99 ± 0.15	ps	JCJ[1], **5**	~20	25	5
1101+384	MRK 421, JVAS J1104+3812	B	0.0308	13.3	722	>100	438 ± 4.21	ps	JCJ[9,32], **4**	~50/~310	323	13
1105+437	B3 1105+437, JVAS J1108+4330	Q	1.226	19.5	375	5.92	0.33 ± 0.16		R[1,27], **1**	/	227	/
1106+380	B2 1106+38, CLASS J1109+3744	G	2.29	23.0?[r]	867	2.86	0.22		U[4], **0**	/	16	/
1107+607	JVAS J1110+6028				404	0.21	0.04		U[1,27], **0**	/	27	/
1124+455	B3 1124+455, JVAS J1126+4516	Q[r]	1.811	17.0	355	22.26	0.95 ± 0.25	s	U[1,27], **0**	/	351	/
1124+571	S4 1124+57, JVAS J1127+5650	Q	2.890	19.0	597	5.19	0.13		U[10], **0**	/	82	/
1125+596	TXS 1125+596, JVAS J1128+5925	Q	1.779	20.0	393	23.78	0.44 ± 0.11	s	U[1], **0**	/	261	/
1128+385	B2 1128+38, JVAS J1130+3815	Q	1.733	19.4	746	12.11	0.62 ± 0.24	s	J[3], **2**	175	241	66
1143+590	JVAS J1146+5848	Q	1.982	19.6	674	5.08	0.70		U[1], **0**	/	62	/
1144+542	S4 1144+54, JVAS J1146+5356	Q	2.201	20.5	484	3.83	0.16		U[1], **0**	/	186	/
1144+402	B3 1144+402, JVAS J1146+3958	Q	1.088	18.5	739	4.73	0.47		J[2], **2**	35	~10	25
1144+352	B2 1144+35B, JVAS J1147+3501	G	0.063	15.7	663	10.34	0.62 ± 0.23	s	JCJ[20], **4**	120	~300	180
1146+596	NGC 3894, JVAS J1148+5924	G	0.0108	11.0	627	2.40	0.23		U[1], **0**	/	~140	/
1150+812	8C 1150+812, JVAS J1153+8058	LPQ	1.250	18.5	1181	4.88	0.46 ± 0.03	p	J[3], **2**	260	167	93
1151+408	B3 1151+408, JVAS J1153+4036	Q	0.916	19.5	380	1.22	0.18		J[1], **2**	30	90	60
1155+486	TXS 1155+486, JVAS J1158+4825	Q	2.028	19.9	445	3.33	0.41		J[1], **2**	192	256	64
1205+544	JVAS J1208+5413				397	1.25	0.14		U[1], **0**	/	120/225	/
1206+415	B3 1206+416, JVAS J1209+4119	B		16.3	515	36.39	1.21 ± 0.25	s	U[1,27], **0**	/	196	/
1213+350	4C +35.28, JVAS J1215+3448	Q	0.857	20.1	1152	8.6	0.22 ± 0.09		[15,23], **?**	25	55/235	30
1216+487	S4 1216+48, JVAS J1219+4829	Q	1.076	18.5	680	3.39	0.18		JCJ[1], **3**	80/105/285	104	1
1218+444	B3 1218+444B, JVAS J1221+4411	Q	1.345	17.3	478	2.69	0.13		U[1], **0**	/	318	/
1221+809	8C 1221+809, JVAS J1223+8040	B		18.7	518	6.64	0.34 ± 0.17	s	JCJ[1], **3**	353/215	354	1
1223+395	B2 1223+39, JVAS J1225+3914	Q[n]	0.623	20.6	438	1.73	0.09		JCJ[1], **3**	50/230	37/207	13/23
1226+373	TXS 1226+373, JVAS J1228+3706	Q	1.515	18.0	953	14.25	0.39 ± 0.13	s	U[1,27], **0**	/	308	/
1239+376	B2 1239+37, JVAS J1242+3720	Q	3.818	19.5	446	0.60	0.05		J[21], **2**	167	16	151
1240+381	B2 1240+38, JVAS J1242+3751	Q	1.316	19.1	768	6.32	0.24 ± 0.11		U[1,4,27], **0**	/	113	/
1246+586	PG 1246+586, JVAS J1248+5820	B		14.0	414	>100	6.50 ± 0.47	s	U[1,27], **0**	/	2	/

Table 1. continued.

CJF name		type	z	m_v	S_m [mJy]	EXML	$f_x \times 10^{-12}$ [erg/cm^2/s]	OBS	VLA structure	$\theta_{\rm VLA}$ [deg]	$\theta_{\rm VLBI}$ [deg]	ΔPA [deg]
(1)	(2)	(3)	(4)	(5)	(6)	(7)	(8)	(9)	(10)	(11)	(12)	(13)
1250+532	TXS 1250+532, JVAS J1253+5301			16.4	396	11.31	0.52 ± 0.17	s	J[1,27], **2**	14,200	253	53
1254+571	MRK 231, JVAS J1256+5652	Q,pec Sy1	0.04217	14.41	419	6.29	0.21 ± 0.12	p	SA(rs)c?, U[1,28], **0**	/	/	/
1258+507	TXS 1258+507, JVAS J1300+5029	Q	1.561	22.2[r]	391	6.88	0.29 ± 0.13		J[1], **2**	170	166	4
1300+580	JVAS J1302+5748	G[r]	1.088[r]	21.1[r]	758	12.37	0.41 ± 0.14	s	U[1,27], **0**	/	14	/
1305+804	8C 1305+804, J130605.6+800820	Q	1.183		375	19.93	0.89 ± 0.25	s	/	/	60	/
1306+360	[VCV2001] J130823.7+354637	Q?[r]	1.055[r]	20.4[r]	437	11.51	0.42 ± 0.14	s	/	/	348	/
1307+562	JVAS J1309+5557	Q	1.629	17.6	416	30.66	0.95 ± 0.18	s	R[1], **1**	/	192	/
1308+471	JVAS J1310+4653		1.113	19.1	393	8.38	0.24 ± 0.11		U[1,27], **0**	/	/	/
1309+555	TXS 1308+554, JVAS J1311+5513	Q	0.926	19.1	677	11.58	0.29 ± 0.11	s	J[1], **2**	?	346	/
1312+533	JVAS J1314+5306				433	2.49	0.15		U[1], **0**	/	242	/
1322+835	S5 1322+83, VCS1 J1321+8316		1.024,t[r]		506	4.11	0.20		R[1], **1**	70	~310	120
1323+800	S5 1323+79, [VCV2001] J132351.6+794252	G	1.97	21.5	458	2.87	0.22		U[1], **0**	/	89	/
1321+410	JVAS J1324+4048	G[r]	0.496	19.5	413	1.36	0.09		U[1], **0**	/	~280	/
1325+436	B3 1325+436, JVAS J1327+4326	Q	2.073	20.0	533	5.59	0.19		U[1,27], **0**	/	225	/
1333+459	S4 1333+45, JVAS J1335+4542	Q	2.449	18.5	598	6.22	0.32 ± 0.13	s	U[1,10,27], **0**	/	295	/
1333+589	JVAS J1335+5844	G		21.9	820	10.23	0.34 ± 0.12		U[1,27], **0**	/	~20	/
1335+552	JVAS J1337+5501	Q	1.096	19.0	811	11.15	0.41 ± 0.14	s	R[1,27], **1**	45	~110	65
1337+637	JVAS J1339+6328	Q	2.558	18.5	431	3.10	0.10		U[1], **0**	/	213	/
1342+663	S4 1342+663, JVAS J1344+6606	Q	1.351	20.0	510	1.75	0.10		J[1], **2**	136	/	/
1347+539	4C +53.28, JVAS J1349+5341	Q	0.980	17.3	635	15.97	0.58 ± 0.17	s	JCJ[1], **4**	317	138	179
1355+441	B3 1355+441, CLASS J1357+4353	G[r]	0.646[r]	21.0 [r]	464	1.94	0.12		/	/	296	/
1357+769	S5 1357+76, JVAS J1357+7643	B[r]		19.4	844	0.45	0.05		U[1], **0**	/	249	/
1356+478	S4 1356+47, CLASS J1358+4737	G	0.230	19.5	428	0.00	0.00		/	/	247	/
1413+373	JVAS J1415+3706	Q	2.36	18.33	383	1.49	0.30 ± 0.04	p	U[1], **0**	/	126	/
1415+463	4C +46.29, JVAS J1417+4607	Q	1.552	17.9	904	34.46	0.42 ± 0.09	s	JCJ[1], **4**	259	260	1
1418+546	PG 1418+546, JVAS J1419+5423	B	0.151	15.65	1707	>100	1.44 ± 0.19	ps	J[2], **3**	263	127	136
1417+385	B3 1417+385, JVAS J1419+3821	Q	1.832	19.3	871	19.46	0.40 ± 0.11	s	U[1], **0**	/	/	/
1421+482	JVAS J1423+4802	Q	2.220	18.9	536	0.71	0.07		U[1], **0**	/	278	/
1424+366	JVAS J1426+3625	B	1.091	18.3	429	2.06	0.11	s	J[1], **2**	189	227	38
1427+543	S4 1427+543, JVAS J1429+5406	Q	2.991	19.8	718	13.27	0.36 ± 0.11	s	U[1], **0**	/	138	/
1432+422	B3 1432+422, JVAS J1434+4203	Q	1.240	17.8	353	2.38	0.12		U[27], **0**	/	~100	/
1435+638	S4 1435+63, JVAS J1436+6336	Q	2.068	15.0	795	14.20	1.09 ± 0.34	ps	J[16], **3**	230	215	15
1438+385	CLASS J1440+3820	Q	1.775	21.6	944	0.29	0.05		cD[1,27], **3**	~350	~350	0
1442+637	JVAS J1443+6332	Q	1.380	17.3	456	5.78	0.48 ± 0.06	p	U[1], **0**	/	183	/
1448+762	S5 1448+76, JVAS J1448+7601	Q	0.899	22.3	683	1.16	0.08		U[1], **0**	/	83	/
1456+375	JVAS J1458+3720	G	0.333	18.2	591	0.77	0.03		U[1], **0**	/	118	/
1459+480	TXS 1459+480, JVAS J1500+4751	B[r]	1.059[r]	19.9 [r]	489	3.29	0.21		J[1], **2**	?	79	/
1504+377	S4 1504+377, JVAS J1506+3730	G,Sy2	0.6715	21.2	1003	3.76	0.14		J[23], **2**	83	224	141
1505+428	B3 1505+428, JVAS J1506+4239	G[r]	0.587	19.4 [r]	404	11.11	0.50 ± 0.16	s	J[1], **3**	250–270[1]	259	0
1526+670	JVAS J1526+6650	Q	3.02	17.2	417	9.82	0.22 ± 0.08	s	U[1,27], **0**	/	45	/
1531+722	S5 1531+72, JVAS J1531+7206	Q	0.899	17.7	452	25.44	0.41 ± 0.11	s	J[1], **2**	56	288	128
1534+501	JVAS J1535+4957	Q	1.121	18.0	359	0.97	0.07		U[1], **0**	/	325	/
1543+517	JVAS J1545+5135	Q	1.924	17.3	544	25.50	0.50 ± 0.12	s	J[1], **2**	180	178	2
1543+480	JVAS J1545+4751	Q	1.277	21.7	441	2.27	0.09		U[1], **0**	/	131	/
1545+497	4C +49.26, JVAS J1547+4937	G	0.70	19.6	549	1.32	0.08		J[1], **3**	340	/	/
1547+507	S4 1547+50, JVAS J1549+5038	Q	2.169	18.5	724	49.91	0.74 ± 0.13	s	J[1], **2**	120	215	95
1550+582	7C 1550+5815, JVAS J1551+5806	Q	1.324	16.7	367	70.16	0.79 ± 0.12	s	U[1,27], **0**	/	156	/
1619+491	JVAS J1620+4901	Q	1.513	17.8	469	6.04	0.50 ± 0.21		U[1,27], **0**	/	~15	/
1622+665	JVAS J1623+6624	G	0.201	17.2	520	36.95	0.60 ± 0.11	s	U[27], **0**	/	57	/
1623+578	7C 1623+5748, JVAS J1624+5741	G	0.789	17.3	590	8.61	0.22 ± 0.08	s	U[27], **0**	/	254	/
1624+416	4C +41.32, JVAS J1625+4134	LPQ	2.550	22.	1362	4.84	0.11± 0.04	**p**	J[1], **2**	351	239	112
1629+495	JVAS J1631+4927	Q	0.52	18.3	394	16.02	0.56 ± 0.15	s	JCJ[1], **3**	~245–270	~245	0
1633+382	B3 1633+382, JVAS J1635+3808	LPQ	1.807	18	3189	12.87	0.31 ± 0.10	ps	JCJ[3], **4**	165/9	283	86
1636+473	B3 1636+473, JVAS J1637+4717	Q	0.740	17.5	1330	24.85	0.55 ± 0.13	ps	J[1,16], **3**	10–30	334	36–56
1637+574	S4 1637+57, JVAS J1638+5720	LPQ	0.749	17.	1807	>100	2.12 ± 0.23	ps	J,H[2,3], **4**	270–280	200	70–80
1638+540	JVAS J1639+5357	Q	1.977	19.7	369	4.40	0.04 ± 0.01	p	U[1], **0**	/	206	/
1638+398	B3 1638+398, JVAS J1640+3946	Q	1.66	16.5	1285	2.42	0.15 ± 0.03	p	JCJ[1], **3**	145	/	/
1642+690	S4 1642+69, JVAS J1642+6856	HPQ	0.751	19.2	1516	59.99	0.68 ± 0.10	s	JCJ,H[3], **5**	168	191	23
1641+399	3C 345, GB6 J1642+3948	Q	0.595	15.96	8363	>100	3.96 ± 0.29	ps	J,H[3], **5**	328	230	98
1645+635	87GB 1645+63, JVAS J1645+6330	Q	2.379	19.4	444	1.94	0.09		J[1], **2**	132	~30	102
1645+410	87GB 1645+41, JVAS J1646+4059	Q	0.835	20.7	388	9.92	0.36 ± 0.13		U[1], **0**	/	~130	/
1652+398	MRK 501, JVAS J1653+3945	B	0.03366	14.15	1371	>100	80.15 ± 1.49	ps	JCJ,H[1,6], **4**	49	132	83
1656+571	4C +57.28, JVAS J1657+5705	HPQ	1.281	17.4	844	27.41	0.65 ± 0.15	ps	JCJ[1,16,27], **3**	52	54	2
1656+482	4C +48.41, JVAS J1657+4808	G		20.0 [r]	847	53.82	1.03 ± 0.17	s	JCJ[1,27], **3**	24–37	255	129–142
1656+477	S4 1656+47, JVAS J1658+4737	Q	1.622	18.0	1420	15.31	0.42 ± 0.13	s	U[3,27], **0**	/	344	/
1700+685	87GB 1700+685, JVAS J1700+6830	G	0.301	17.1	435	24.48	0.23 ± 0.05	s	U[1,27], **0**	80	130	50
1716+686	HS 1716+6839, JVAS J1716+6836	Q	0.339	18.5	988	>100	2.95 ± 0.15	s	U[1], **0**	/	328	/
1719+357	S4 1719+35, JVAS J1721+3542	Q	0.263	17.5	874	70.37	1.32 ± 0.22	s	JCJ[1], **5**	175	178	3
1722+401	B3 1722+401, JVAS J1724+4004	Q?[r]	1.049	21.0	532	18.58	0.60 ± 0.16	s	JCJ[1], **4**	228/327	305	22
1726+455	B3 1726+455, JVAS J1727+4530	Q	0.717	19.0	1066	19.66	0.53 ± 0.13	s	J[1], **2**	326–345	278	48–67
1732+389	IRAS 17326+3, JVAS J1734+3857	Q[r]	0.97	19.0	561	3.94	0.15	ps	J[1], **2**	180	110	70
1734+508	S4 1734+508, JVAS J1735+5049	G?	0.835[r]	22.4[r]	798	2.83	0.08		U[1], **0**	/	18	/
1738+499	S4 1738+499, JVAS J1739+4955	Q	1.545	19.0	478	15.48	0.43 ± 0.11	s	R[1], **1**	16	23	7
1738+476	S4 1738+47, JVAS J1739+4737	B	0.950	19.5	789	13.06	0.44 ± 0.12	s	U[1,27], **0**	/	250	/
1739+522	4C +51.37, JVAS J1740+5211	HPQ	1.381	18.5	1133	60.93	0.93 ± 0.15	s	J[16], **2**	261	7	106
1744+557	NGC 6454, CLASS J1744+5542	G	0.0306	14.5	599	>100	0.91 ± 0.12	s	JCJ[24], **4**	70/257	248	9
1745+624	4C +62.29, JVAS J1746+6226	Q	3.889	19.5	580	>100	0.72 ± 0.08	ps	J[1], **2**	228	211	17
1746+470	JVAS J1747+4658			21.3	634	14.79	0.39 ± 0.11	s	U[1,27], **0**	/	270	/

Table 1. continued.

CJF name		type	z	m_v	S_m [mJy]	EXML	$f_x \times 10^{-12}$ [erg/cm^2/s]	OBS	VLA structure	$\theta_{\rm VLA}$ [deg]	$\theta_{\rm VLBI}$ [deg]	ΔPA [deg]
(1)	(2)	(3)	(4)	(5)	(6)	(7)	(8)	(9)	(10)	(11)	(12)	(13)
1749+701	HS 1749+7006, JVAS J1748+7005	B	0.7699	17.01	728	>100	1.41 ± 0.09	ps	J[1], **2**	25	308	77
1747+433	JVAS J1749+4321	B		17.0	367	12.61	0.38 ± 0.12	s	J[1], **2**	180	170	10
1751+441	B3 1751+441, JVAS J1753+4409	Q	0.871	19.5	998	28.77	0.69 ± 0.15	s	JCJ[1], **5**	77	85	8
1755+578	JVAS J1756+5748	Q	2.110	18.0	455	24.10	0.37 ± 0.08	s	U[1,27], **0**	/	260	/
1758+388	S4 1758+38, JVAS J1800+3848	Q	2.092	18.0	722	57.94	1.33 ± 0.22	s	R[1], **1**	255	265	10
1803+784	S5 1803+78, JVAS J1800+7828	B	0.6797	17.	2633	>100	1.63 ± 0.18	ps	J[3,6], **3**	195	265	70
1800+440	B3 1800+440, JVAS J1801+4404	Q	0.663	17.5	1148	77.54	1.48 ± 0.20	s	JCJ[1,16,27], **4**	240	205	35
1807+698	3C 371, JVAS J1806+6949	B	0.051	14.4	2189	>100	3.40 ± 0.13	ps	J,H[6], **4**	241	264	23
1809+568	JVAS J1810+5649	Q?[r]	2.041[r]	19? [r]	576	11.30	0.19 ± 0.07	s	U[1], **0**	/	324	/
1812+412	B3 1812+412, JVAS J1814+4113	Q	1.564	18.9	534	4.57	0.20		J[27], **2**	325–250	80	115–170 curv.
1818+356	S4 1818+35, [VCV2001] J182042.1+354040	Q	0.971	21.1	573	5.87	0.26	s	/	/	143	/
1826+796	S5 1826+79, JVAS J1823+7938	G	0.224	16.7	577	2.16	0.07		U[1], **0**	/	242	/
1823+568	4C +56.27, JVAS J1824+5651	B	0.664	18.4	1135	>100	2.25 ± 0.17	ps	J,H[3], **5**	98	197	99
1828+399	JVAS J1829+3957			15.3	353	2.44	0.17		U[1], **0**	/	302	/
1834+612	JVAS J1835+6119	Q	2.274	17.6	590	17.89	0.27 ± 0.08	s	J[1], **3**	154	190	36
1839+389	B3 1839+389, JVAS J1840+3900	Q	3.095	19.5	476	3.21	0.23		U[1], **0**	/	359	/
1842+681	S4 1842+68, JVAS J1842+6809	Q	0.472	17.9	936	>100	1.36 ± 0.13	s	J,H[1], **4**	~290	134	156
1843+356	JVAS J1845+3541	G?	0.764	21.9	794	1.70	0.09		U[1], **0**	/	45	/
1849+670	JVAS J1849+6705	Q	0.657	18.0	992	>100	0.86 ± 0.10	s	JCJ[1], **3**	240	306	66
1851+488	S4 1851+48, JVAS J1852+4855	Q	1.25	19.0	351	1.20	0.12		U[1], **0**	/	/	/
1850+402	S4 1850+40, JVAS J1852+4019	Q	2.12	18.5	535	2.93	0.20		J[1], **2**	327	235	92
1856+737	JVAS J1854+7351	Q	0.461	17.5	546	>100	2.03 ± 0.19	s	J[1], **3**	24	30	6
1908+484	JVAS J1909+4834	Q	0.513	19.0	423	6.40	0.33 ± 0.16		cJ[1], **5**	90 +	51	39
1910+375	JVAS J1912+3740	Q	1.104	18.5	402	3.15	0.21		R[1], **1**	?	176	/
1924+507	4C +50.47, JVAS J1926+5052	Q	1.098	17.9	354	17.70	0.87 ± 0.25	s	cJCJ[1,29], **4**	9	2	7
1926+611	87GB 1926+611, JVAS J1927+6117	B	>0.2	17.5	618	21.64	0.58 ± 0.13	s	J[1], **2**	195	127	68
1928+738	4C +73.18, JVAS J1927+7358	LPQ	0.302	16.5	3561	>100	9.10 ± 0.48	ps	cJCJ[3], **5**	189	167	22
1936+714	S5 1936+71, JVAS J1936+7131	Q	1.864	19.5	391	1.05	0.08		J[1], **2**	351	189	162
1943+546	S4 1943+54, JVAS J1944+5448	G	0.263	17.6	938	5.22	0.23		U[1], **0**	/	81	/
1946+708	87GB 1946+704, JVAS J1945+7055	G	0.101	16.1	645	1.95	0.11		U[1], **0**	/	205	/
1950+573	JVAS J1951+5727	G[r]	0.652	18.0	476	7.36	0.58 ± 0.24	s	U[1,27], **0**	/	74	/
1954+513	S4 1954+51, JVAS J1955+5131	LPQ	1.223	18.5	1610	48.30	1.86 ± 0.34	s	JCJ[1], **4**	345/180	302	43
2007+777	S5 2007+77, JVAS J2005+7752	B	0.342	16.5	1279	48.53	1.01 ± 0.19	ps	JCJ[3], **4**	90/250	264	14
2005+642	JVAS J2006+6424	Q?	1.574	19.0	739	10.8	0.31 ± 0.12	s	U[1], **0**	/	/	/
2007+659	TXS 2007+659, JVAS J2007+6607	Q	1.325	16.4	756	3.90	0.23		J[1], **2**	322	210	112
2010+723	4C +72.28, JVAS J2009+7229	B	>0.2	19.0	910	3.16	0.39		J[1], **2**	103	320–230	127–143
2017+745	4C +74.25, JVAS J2017+7440	Q	2.187	18.3	500	26.66	1.00 ± 0.24	s	J[1], **2**	180	90	90
2021+614	87GB 2021+612, JVAS J2022+6136	LPQ	0.227	19.5	2743	4.91	0.36		U[1], **0**	/	~35	/
2023+760	S5 2023+76, JVAS J2022+7611	B	>0.2	17.8	426	2.55	0.09		J[1], **2**	?	209	/
2054+611	JVAS J2055+6122	Q?[r]	0.864[r]	21.5?[r]	414	5.42	0.55		U[1], **0**	/	161	/
2116+818	S5 2116+81, JVAS J2114+8204	Q,Sy1	0.084	15.7	376	>100	11.44 ± 0.61	s	/	/	333	/
2136+824	S5 2136+82, JVAS J2133+8239	Q	2.357	18.9	509	4.91	0.39		J[1], **2**	133	143	10
2138+389	JVAS J2140+3911		1.306,t[r]	19.0	502	3.50	0.54	s	U[1], **0**	/	91	/
2200+420	BL Lacertae, JVAS J2202+4216	B	0.0686	14.5	3593	>100	4.33 ± 0.62	ps	JCJ[7], **4**	~150/~300	~180	30
2214+350	B2 2214+35, JVAS J2216+3518	Q	0.510	18.0	477	6.53	0.45 ± 0.24		J[1], **3**	212	173	39
2229+695	S5 2229+69, JVAS J2230+6946	B	1.413,t,[r]	19.6	1365	0.38	0.15		JCJ[1], **3**	70/167	~70	0
2235+731	JVAS J2236+7322	Q	1.345	21.5?	424	3.21	0.63		U[1], **0**	/	39	/
2238+410	JVAS J2241+4120	B?[r]	0.726[r]	17.9	677	5.01	0.51		J[1], **2**	277	135	142
2253+417	B3 2253+417, JVAS J2255+4202	Q	1.476	18.8	1120	10.67	1.06 ± 0.36	s	U[1,27], **0**	/	~40	/
2255+416	4C +41.45, JVAS J2257+4154	Q	2.15	20.9	1111	3.95	0.39		R[1], **1**	180	179	1
2259+371	JVAS J2301+3726	Q	2.179	20.4	406	1.91	0.22		JCJ[1], **3**	19	7	12
2309+454	JVAS J2311+4543	Q	1.447	20.0? [r]	597	1.23	0.18		U[1], **0**	/	122	/
2310+385	B3 2310+385, JVAS J2312+3847	Q	2.181	17.5	484	3.03	0.23		U[1], **0**	/	238	/
2319+444	JVAS J2322+4445	G [r]	1.251[r]	19.9	366	0.31	0.17		J[1], **2**	109	344	125
2346+385	B3 2346+385, JVAS J2349+3849	Q	1.032	19.1	640	21.63	1.97 ± 0.57	s	J[1], **2**	263	329	66
2351+456	4C +45.51, JVAS J2354+4553	LPQ	1.986	20.6	1145	5.49	0.47		J[1,27], **2**	200	288	88
2352+495	JVAS J2355+4950	G	0.237	20.1	1552	0.44	0.14		U[1], **0**	/	163	/
2353+816	S5 2353+81, JVAS J2356+8152	B	1.344	20.3	476	2.66	0.31		JCJ[1], **2**	63	341	82
2356+390	B3 2356+390, JVAS J2358+3922	Q, C.g.l.	1.198	20.6	371	10.0	0.71 ± 0.03	s	J[1,27], **2**	336	230	106
2356+385	S4 2356+38, JVAS J2359+3850	Q	2.704	19.0	449	7.97	1.27 ± 0.48	s	R[1], **1**	90	180	90

surface-brightness threshold of the VLA maps. The large-scale position angles have been measured from the published maps.

In Col. 11 we give the position angle of the VLA jet ($\theta_{\rm VLA}$), followed by the position angle of the VLBI jet (Col. 12, $\theta_{\rm VLBI}$). Column 13 lists the difference between the two position angles (ΔPA). A "/" in Col. 10 or 11 denotes that no information is available on the large-scale structure, and in Col. 12, on a point-like structure in the VLBI-scale structure. In several cases two values are given in Cols. 11, 12, or 13 indicating jet and counter-jet position angles. For further calculations we used the position angle difference determined for the one of these with higher total flux-density. For more complete information on the pc-scale radio properties of the sources we refer to Paper II for details on the jet-component kinematics and to Paper I for details on the VLBI maps and model-fits.

4.1. X-ray properties of the sample

Before discussing the broad-band properties of individual subclasses of objects we will give a general overview of the source content of the sample. In total, the CJF-survey consists of 293 sources; 167 have been detected by *ROSAT* and 126 have not been detected. The CJF contains 198 quasars (including Seyfert 1s), of which 93 were not detected in the RASS survey,

Table 2. References and abbreviations for Table 1.

/ no VLA information found

[1] T. Pearson
[2] Price et al. (1993)
[3] Murphy et al. (1993)
[4] Vigotti et al. (1989)
[5] Baum et al. (1990)
[6] Cassaro et al. (1999)
[7] Antonucci (1986)
[8] Peacock & Wall (1982)
[9] Antonucci & Ulvestad (1985)
[10] Neff & Hutchings (1990)
[11] Wagner et al. (1996)
[12] Pedlar et al. (1983)
[13] Pedlar et al. (1990)
[14] Patnaik et al. (1993)
[15] Browne & Perley (1986)
[16] Reid et al. (1995)
[17] Machalski et al. (1982)
[18] Garrington et al. (1991)
[19] Barthel et al. (1986)
[20] Giovannini et al. (1999)
[21] Machalski (1998)
[22] Machalski & Condon (1983)
[23] Perley (1982)
[24] Bridle & Fomalont (1978)
[25] Kühr et al. (1986)
[26] Hummel et al. (1997)
[27] Patnaik et al. (1992)
[28] Thean et al. (1999)
[29] Owen & Puschell (1984)
[30] Machalski et al. (1996)
[31] Perley et al. (1982)
[32] Ulvestad et al. (1983)

[m] : Marcha et al. (1996)
[r] : priv. comm. R. Vermeulen
[n] : NED information

U:	unresolved component	R:	slightly resolved component
(c)J:	(complex) jet-like extended component	(c)D:	(complex) double source
(c) JCJ:	(complex) jet- and counter-jet	H:	halo emission
G_L:	gravitational lens system	C.g.l.	Candidate gravitational lens

[#] Kim et al. (1991)
[$] Slee & Siegman (1983)

53 radio galaxies (including Seyferts) of which 33 were not detected, 32 BL Lacs (8 non-detections), and 10 objects which have not yet been classified. The highest rate of non-detection is among the radio galaxies, whereas most of the BL Lacs have been found as strong X-ray emitters. In Fig. 1a we show the redshift distributions of the CJF sources detected (solid black line) and not detected (shaded) by *ROSAT*. The biggest difference between the two distributions is among the nearby objects: lower z objects ($0 < z < 0.7$) seem to have a higher likelihood to be detected by *ROSAT*.

Figures 1b−d show the distribution of Fig. 1a separately for the three different classes of objects. In the case of the quasar distribution, higher-z quasars are (preferentially) detected. BL Lac objects show the highest rate of detections among the low-z objects. However, BL Lac objects are less numerous and only appear in the CJF at smaller redshifts than the quasars. The number of low-z detected and non-detected radio galaxies is identical.

The count rates determined individually as described above are generally consistent (inside the mutual errors) with the results of the standard processing of the RASS data. Of particular interest is the group of 54 objects for which pointed observations have been performed in the years after the All Sky Survey. Figure 2 shows the count rate during the pointed observations as a function of the count rates obtained from the survey data. One object, the BL Lac object Mrk 421 is outside the upper plot boundary. Arrows at the symbols indicate 2σ upper limits for sources non-detected in the survey observations. The agreement between the two count rates is excellent; larger differences between the individual observations must be attributed mainly to variability of the objects. It should be noted that some quasars and BL Lac objects, observed repeatedly in pointed observations, show variations of their count rates by a factor of two to three, often accompanied by spectral changes as well. For example, both the two extreme BL Lac objects Mrk 421 (1101+384) and Mrk 501 (1652+398) are known to show flux variations of about 50% in different *ROSAT* observations.

In Fig. 3 we plot the K-corrected monochromatic X-ray luminosities (at 2 keV) as a function of the 5 GHz radio luminosities for different classes of objects in the sample. The arrows denote upper limits of non detected objects. Three sources – the radio galaxies 0651+410 and 1146+596 and the BL Lac object 1357+769 – have upper limits below the plot boundary and thus the tentative identification of 1357+769 as BL Lac object might have to be revised.

Interestingly, most of the objects (the radio galaxies included) exhibit a nearly linear relation between X-ray and radio luminosities suggesting a common mechanism for the production of X-ray and radio photons. In addition, we find a trend for the quasars to collect preferentially towards the upper part of the linear distribution while the radio galaxies seem to collect at the lower part. Far above this general trend in Fig. 3 we find the three extreme BL Lac objects Mrk 421, Mrk 501 (at low radio luminosities), and 3C 66A. These three sources belong to the class of HBL where the X-ray emission is thought to be due to synchrotron radiation. The three Seyfert galaxies 2116+818, 0402+379, and 0309+411 show excess X-ray emission at low radio luminosities. 0251+393 was classified as quasar by Marcha et al. (1996) and appears even as quasar overluminous in X-rays.

Similar behaviour is seen in the plot of the optical vs. the X-ray luminosities (Fig. 4). The source 1357+769 appears to be extremely under-luminous, both in X-rays and in the optical and falls outside the lower plot boundaries. Thus, either its classification as BL Lac object or its redshift might be incorrect. Further, the upper limit for the X-ray luminosity of the optically rather bright galaxy 1456+375 falls below the plot boundary of Fig. 4. The remarkably strong correlation between radio and X-ray luminosity and the weaker correlation between the radio and the optical luminosity have been discussed earlier by e.g., Browne & Murphy (1987).

4.1.1. Quasars

Flat-spectrum radio quasars are brighter in X-rays than are steep-spectrum objects of comparable optical luminosities

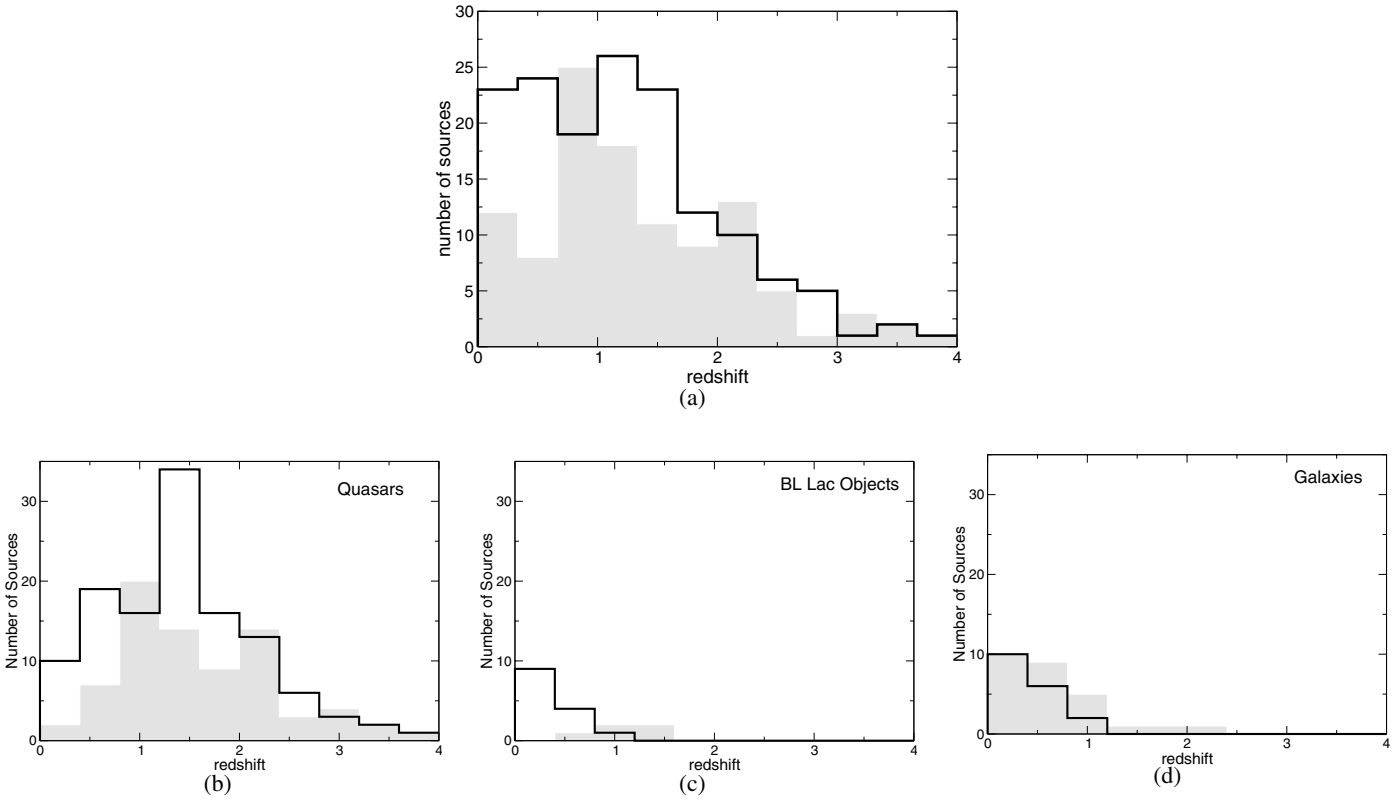

Fig. 1. a) shows the distribution of CJF sources with redshift. The source sample that has been detected by *ROSAT* is indicated by the solid line whereas the distribution of the non-detected source sample is shown in grey. The histograms **b)–d)** show the different z-N distributions for the three classes of objects: **b)** quasars, **c)** BL Lac objects, **d)** radio galaxies; the detected objects are shown by the black line, the non-detections are shown in grey.

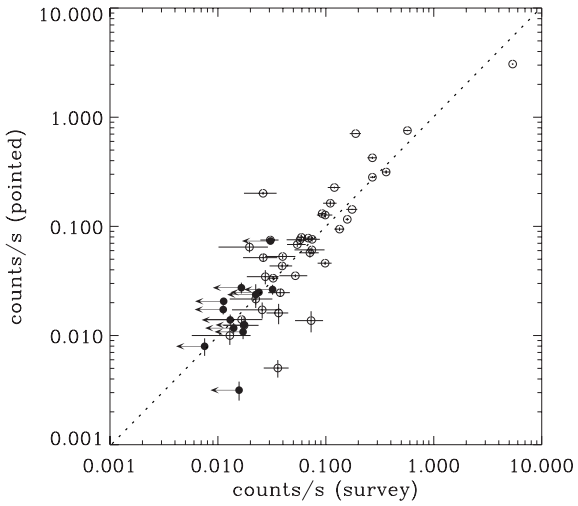

Fig. 2. Comparison of count rates obtained in pointed observations with count rates from the All Sky Survey. The arrows denote upper limits. The equality line is shown dotted.

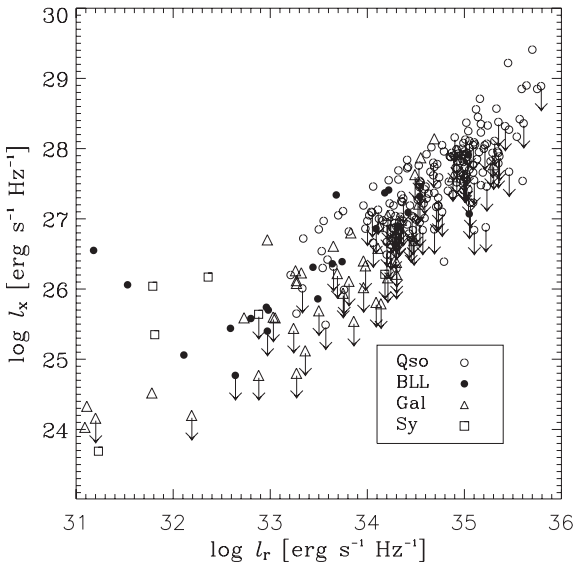

Fig. 3. The monochromatic X-ray luminosity (at 2 keV) as a function of the radio luminosity. The arrows denote the upper limits of non-detected objects.

(Brinkmann et al. 1997). The X-ray loudness $\alpha_{ox} = -0.384 \log (l_{2\ keV}/l_{2500\ Å}) - l_x$ and l_o, respectively, in Fig. 4 – has been used frequently in the past for the discussion of the relative fraction of X-ray to optical emission in an evolving quasar source population. The average value $\langle\alpha_{ox}\rangle = 1.28$ found for the CJF quasars is nearly identical to the result of Brinkmann et al. (1997) for much larger sample of flat spectrum quasars. However, the dispersion in Fig. 5 is rather large and the lower limits with $\alpha_{ox} > 1.7$ indicate that these quasars are either highly variable or X-ray quiet, like BAL quasars (Brinkmann et al. 1999). A further study of these sources is highly desirable. First results from XMM-Newton observations (Brinkmann et al. 2003) indicate that internal absorption is the main cause for the X-ray quiescence of these objects.

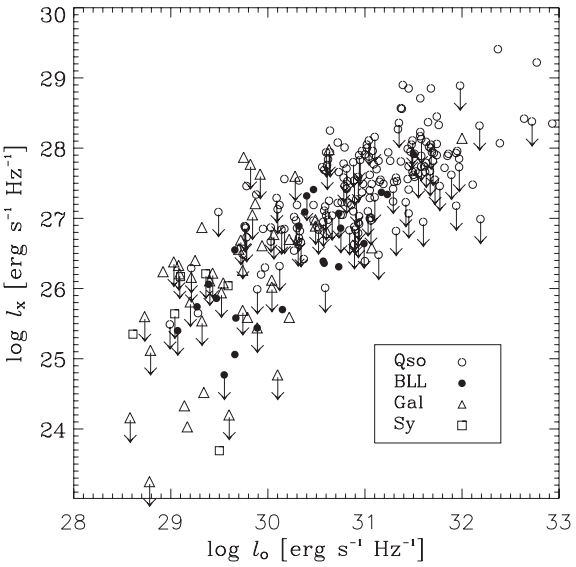

Fig. 4. The monochromatic X-ray luminosity (at 2 keV) as a function of the optical luminosity. The arrows denote the upper limits of non-detected objects.

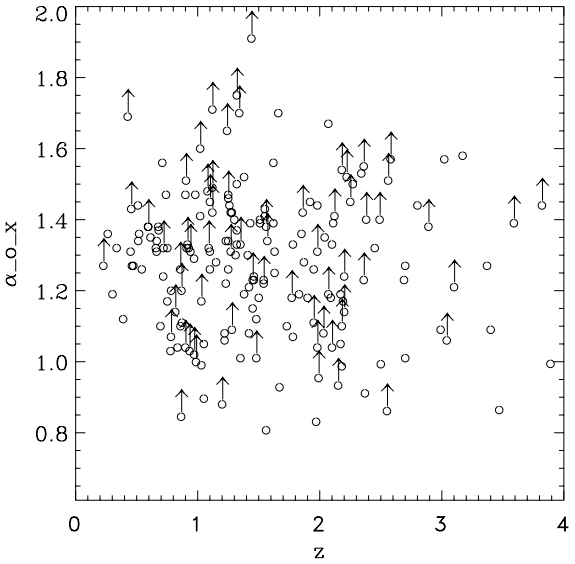

Fig. 5. The X-ray loudness α_{ox} of the quasars as a function of the redshift z. The arrows denote the lower limits of non-detected objects.

4.2. The determination of beaming parameters based on X-ray and radio data

4.2.1. The β_{app}-relation for *ROSAT* detected and non-detected objects

The apparent velocities observed in the core regions of AGN are thought to be caused by relativistic outflows. Relativistic motion of synchrotron-emitting plasma will result in the Doppler boosting of the synchrotron radiation.

We concentrate in this section on those sources where we have obtained the most reliable kinematic information (for details see Paper II). This is a subsample of 150 AGN with 89 sources detected by *ROSAT* (59 Q, 10 B, 10 G, 9 LPQ, 1 HPQ) and 61 non-detected sources (33 Q, 2 B, 19 G, 4 LPQ, 3 HPQ). In order to investigate the evolution of the apparent velocities with redshift for the detected and non-detected sources, we plot this relation in Fig. 6 in panels (a) and (b), respectively. At higher redshifts ($z \geq 1.5$), we find some evidence for a lack of apparently slow sources for the non-detected sources and a tendency towards higher apparent velocities when compared to the detected sources. We plot histograms of β_{app} for the quasars (together with LPQ and HPQ), radio galaxies, and BL Lac objects in panels (c)−(e). The following median values for β_{app} are found for these three classes of objects in the detected sample: $3.33c$, $0.97c$, and $1.83c$, respectively. For the LPQs we find $5.64c$. For the non-detections the values are: $4.47c$ (Q), $0.51c$ (G), and $2.72c$ (B), respectively. For the LPQs and HPQs we find $6.20c$ and $3.29c$, respectively. The numbers of sources are small, nevertheless there is evidence in both samples for higher values for the quasars compared to the radio galaxies. We performed a K-S test comparing the distributions of β_{app} for both the quasars and the radio galaxies. Here and subsequently when we refer to K-S test results, the number quoted is the probability of observing a value the K-S statistic D from two distributions drawn from the same parent that would be higher than the one actually computed; thus a low number means that we can reject the null hypothesis of two similar distributions with high significance. For the comparison of the *ROSAT*-detected subsample, the K-S test yields 0.059, and for the non-detected subsample 0.00013. Radio galaxies show the slowest apparent motions. This is in agreement with the results for the kinematic analysis of the complete survey CJF (see Paper II). The quasars show fastest apparent motions, faster than the BL Lac objects. We find evidence that the detected and non-detected quasars show a different β_{app}-distribution (K-S test: 0.0095) We list the median values in Table 7.

4.2.2. Synchrotron self-compton Limit

A fundamental parameter describing relativistic motion in AGN is the Doppler factor of the flow,

$$\delta = [\Gamma(1 - \beta \cos \phi)]^{-1}, \quad (1)$$

where β is the speed (in units of the speed of light), $\Gamma = (1 - \beta^2)^{-1/2}$ is the Lorentz factor of the flow, and ϕ is the angle between the direction of the flow and the line of sight. Various Doppler factors can be calculated, based on different physical assumptions. Assuming that the observed X-rays are of IC origin, one can compute the IC Doppler factor δ_{IC} (e.g., Jones et al. 1974; Marscher 1987); this equals the real Doppler factor δ of the source flow only if all of the observed X-ray flux is produced through IC scattering. If part of the X-ray flux is produced by some other mechanism, then δ_{IC} is a lower limit to δ. Ghisellini et al. (1993) and Güijosa & Daly (1996) make use of almost the same formalism to derive this Doppler factor for a sample of 105 sources for which the radio and X-ray data were collected from the literature. Here we apply the same formalism to the CJF-data and compare the results with those of Ghisellini et al. and Güijosa & Daly.

Assuming the ideal case of a uniform spherical source of angular diameter θ_d, and a power-law energy distribution of the radiating particles moving in a tangled homogeneous magnetic field (in their rest frame), one can predict the expected IC X-ray flux density, given the relevant radio and X-ray data. Using the observed fluxes this can in turn be used to determine the Doppler factor as

$$\delta_{IC} = f(\alpha) S_m \left[\frac{\ln(\nu_b/\nu_m)\, \nu_x^{\alpha}}{f_x\, \theta_d^{6-4\alpha} \nu_m^{5-3\alpha}} \right]^{1/(4-2\alpha)} (1+z). \quad (2)$$

Here f_x is the observed X-ray flux density (in Jy) at frequency ν_x (keV), ν_m is the frequency at the radio peak (in GHz), θ_d is

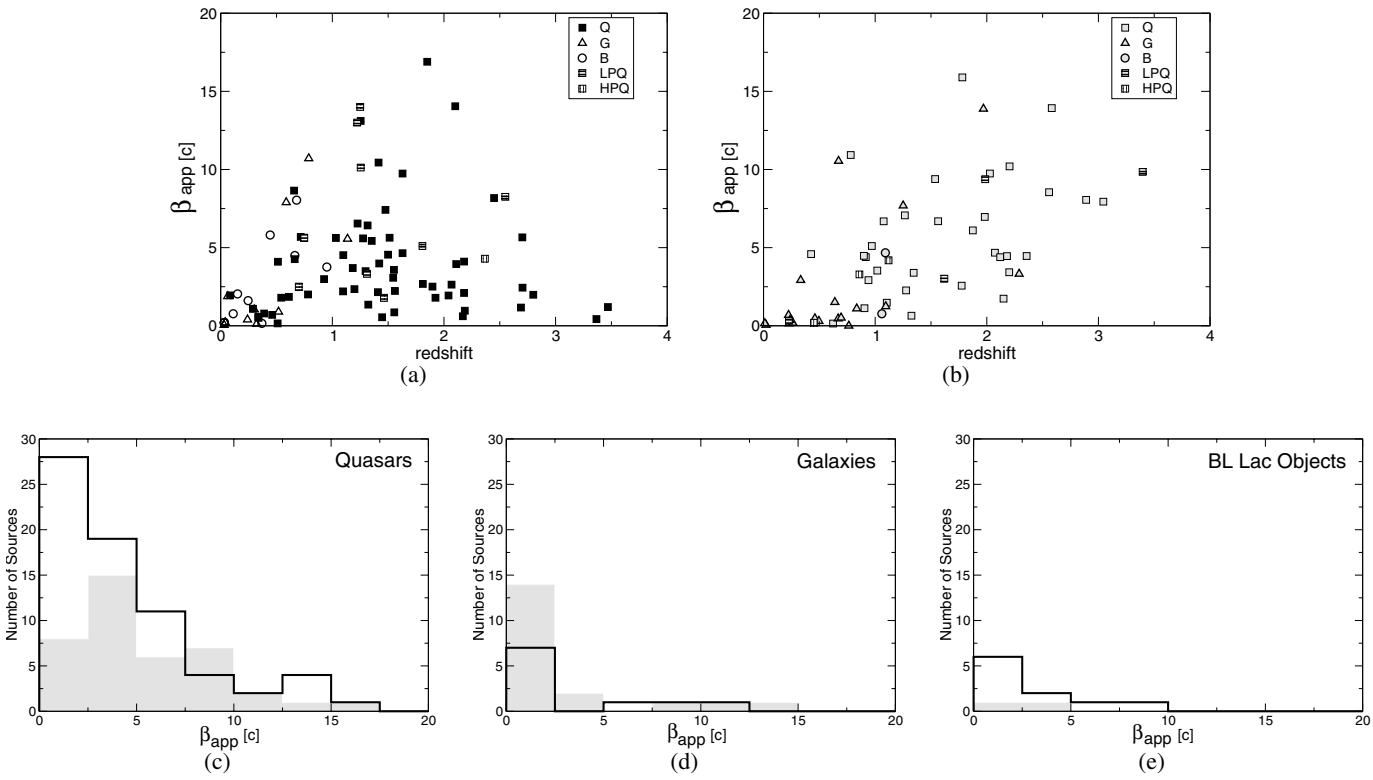

Fig. 6. The $\beta_{\rm app}$-z relation is shown for those sources (source selection explained in the text) detected by *ROSAT* in panel **a)** and those that are non detected in panel **b)** (symbols identical but filled with grey). The figures **c)**–**e)** show the $\beta_{\rm app}$-distribution of the sources in quasars, radio galaxies, and BL Lac objects. The non-detections are shown in grey.

the angular diameter of the source (in milliarcseconds), $\nu_{\rm b}$ is the synchrotron high-frequency cutoff (assumed to be 10^5 GHz), and $f(\alpha) \simeq -0.08\alpha + 0.14$ according to Ghisellini et al. (1987). To convert $f_{\rm x}$ (see Table 1) from erg/cm^2/s to Jy we multiplied $f_{\rm x}$ by a factor of 0.2066×10^{-6} taking emission at 2 keV into account (2 keV $\sim 4.84 \times 10^{17}$ Hz). The flux density $S_{\rm m}$, is the value that would be obtained at $\nu_{\rm m}$ by extrapolating the optically thin spectrum (Marscher 1987). For $\alpha = -0.75$, this is about a factor of 2 larger than the observed peak flux density $S_{\rm op}$ (Marscher 1977, 1987).

Derivation of this formula assumes a single, spherical source. For most AGN, we observe instead a chain of jet components. In this case, according to Ghisellini et al. (1993):

$$\delta_{\rm continuous} = \delta_{\rm sphere}^{(4-2\alpha)/(3-2\alpha)}. \quad (3)$$

All values for the Doppler factors have been calculated twice: once for a uniform spectral index $\alpha = -0.75$ in order to enable a comparison with results presented in the literature, and once for the observationally determined individual spectral indices (Taylor et al. 1996, please see Fig. 7 for the spectral index distribution of the CJF sources). All values are listed in the two Tables 3 and 4. Median values are listed in Table 7.

In Fig. 8 we compare the apparent velocities for the CJF objects with the values for $\delta_{\rm IC}^{\rm con}$ derived from the SSC argument for the same components per source. Panel (a) shows δ calculated using the same spectral index for all sources, and panel (b) using the individual spectral indices taken from Taylor et al. (1996). From this figure and Table 7 we expect to see whether beaming, i.e., the bulk velocity, is sufficient to explain the observed X-ray flux, since the pattern velocity does not contribute to this $\delta_{\rm IC}$.

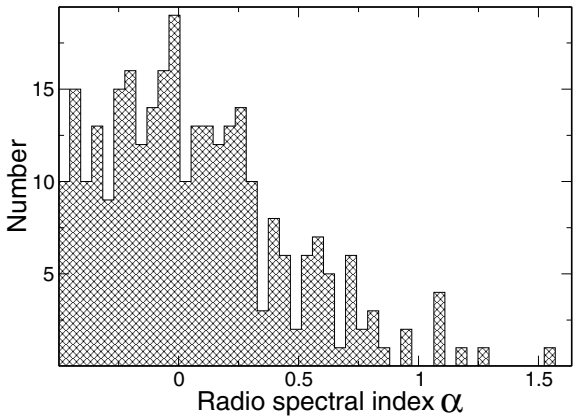

Fig. 7. The distribution of the observed spectral indices is shown (data have been taken from Taylor et al. 1996). The sign convention in Taylor et al. (1996) is different from the sign convention adopted in this paper.

According to Lind & Blandford (1985) and Cohen & Vermeulen (1992), the bulk velocity responsible for the boosting of the radiation could be smaller than the pattern velocity responsible for the superluminal motion (see also Ghisellini et al. 1993). In this case, the average Doppler factor of a sufficiently large sample of sources should be smaller compared to the average apparent velocity. The presented numbers of sources are too small to allow any statistically significant conclusion. For either method of incorporating the spectral indices, we find some evidence for larger values of $\delta_{\rm IC}^{\rm sp}$ and $\delta_{\rm IC}^{\rm con}$ for the quasars compared to the radio galaxies (K-S test: 0.002). This is consistent with Ghisellini et al. (1993), who derived Doppler factors

Table 7. Median values calculated for a set of parameters for those sources that have been detected by *ROSAT*.

	Source class	Q	B	G	LPQ	HPQ
	Number of objects	59	10	10	9	1
	median $\beta_{\rm app}$	3.33c	1.83c	0.97c	5.64c	4.29c
$\alpha = -0.75$	median $\delta_{\rm IC}^{\rm sp}$	1.3	1.0	0.2	1.9	1.4
	median $\delta_{\rm IC}^{\rm con}$	1.4	0.9	0.2	2.2	1.5
observed α	median $\delta_{\rm IC}^{\rm sp}$	3.1	2.1	0.6	3.7	4.8
	median $\delta_{\rm IC}^{\rm con}$	4.4	2.6	0.5	5.3	8.5

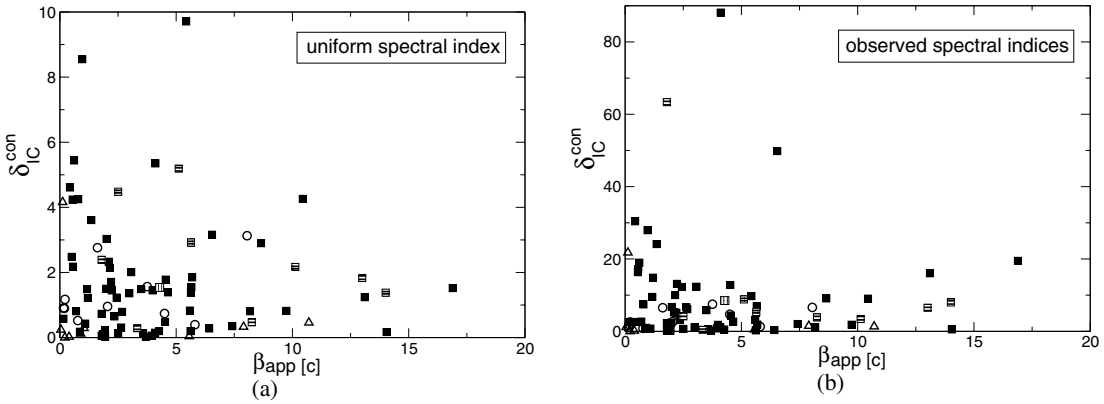

Fig. 8. The panels show the relation between $\beta_{\rm app}$ and $\delta_{\rm IC}^{\rm con}$ for a uniform spectral index **a)** and for the individually determined spectral indices **b)** in those CJF sources detected by *ROSAT*, including only the most reliably determined jet component motions. In both images, the same symbols as in Fig. 6 have been used for the individual source classes.

for about 100 sources with known VLBI structures by comparing predicted and observed X-ray flux in the synchrotron self-Compton model. The derived Doppler factors are largest for core-dominated quasars, intermediate for BL Lac objects, and smallest for lobe-dominated quasars and radio galaxies. For a subsample of 39 superluminal sources, Ghisellini et al. (1993) find that apparent expansion speeds and Doppler factors correlate and have similar average numerical values.

We find a better match between the median $\beta_{\rm app}$ and both $\delta_{\rm IC}$ calculated on the basis of the observed spectral indices compared to a uniformly $\alpha = -0.75$. Although not statistically significant we find a similar median value of $\delta_{\rm IC}$ and $\beta_{\rm app}$ for the quasars and of $\delta_{\rm IC}$ and $\beta_{\rm app}$ for the BL Lac objects. This might support the conclusion that $\delta_{\rm IC}$ and $\beta_{\rm app}$ are of similar value and that there is no need to invoke other scenarios. For a statistically significant investigation of this question clearly a higher number of objects is required, as well as a significantly larger number of VLBI observations for the individual sources.

4.2.3. Equipartition Doppler factors

The equipartition Doppler factors measure the ratio of the particle and magnetic energy densities. By definition is $\delta_{\rm EQ} = \delta_{\rm IC}$ if the source is at equipartition. Otherwise, the ratio $\delta_{\rm EQ}/\delta_{\rm IC}$ measures the source's deviation from equipartition. $\delta_{\rm EQ}$ can be calculated from single-epoch radio observations by assuming that the particles and magnetic field are in equipartition (Readhead 1994). Güijosa & Daly (1996) find a strong correlation between $\delta_{\rm EQ}$ and $\delta_{\rm IC}$ and suggest that they both represent reliable estimates of the true Doppler factor. We use the formula for the equipartition Doppler factor given by Readhead (1994) and Güijosa & Daly (1996):

$$\delta_{\rm EQ} = \left\{[10^3 F(\alpha)]^{34}\left(\left[1-(1+z)^{-1/2}\right]/2h\right)^{-2}(1+z)^{(15-2\alpha)} \times S_{\rm op}^{16}\theta_{\rm d}^{-34}(\nu_{\rm op}\times 10^3)^{-(2\alpha+35)}\right\}^{1/(13-2\alpha)}. \quad (4)$$

The equation as well as a graph for $F(\alpha)$ are given in Scott & Readhead (1977). Here we only need $F(-0.75) = 3.4$. The calculated values for $\delta_{\rm EQ}$ are listed in Table 3 and 4.

In Fig. 9a we show the relation between $\delta_{\rm IC}$ and $\delta_{\rm EQ}$, and we calculate $\delta_{\rm IC}$ for both sphere-like and continuous jets. We find a good correlation between both Doppler factors. The probability that the correlation is spurious is 1×10^{-7} for the continuous jet case and 5×10^{-7} for the sphere-like jet case. $\delta_{\rm IC}$ and $\delta_{\rm EQ}$ are about equal as shown in the histogram displaying the ratio between these two values in Fig. 9b. Both seem to present reliable estimates of the true Doppler factor, as found by Güijosa & Daly (1996). We list the values in Tables 3 and 4. We wish to stress that the calculation of both Doppler factors depends critically on θ_d which is raised to the biggest exponent in Eqs. (2) and (4) when each is re-factored into products of powers of the individual observables, considering the case of uniform $\alpha = -0.75$.

4.2.4. Bulk Lorentz factor and viewing angle

In the ballistic model of knot motion ($\Gamma_{\rm pattern} = \Gamma_{\rm bulk}$), the Lorentz factor Γ and the viewing angle ϕ can be calculated with the help of $\delta_{\rm IC}$ and $\beta_{\rm app}$ (e.g., Ghisellini et al. 1993):

$$\Gamma = \frac{\beta_{\rm app}^2 + \delta_{\rm IC}^2 + 1}{2\delta_{\rm IC}} \quad (5)$$

$$\tan(\phi) = \frac{2\beta_{\rm app}}{\beta_{\rm app}^2 + \delta_{\rm IC}^2 - 1}. \quad (6)$$

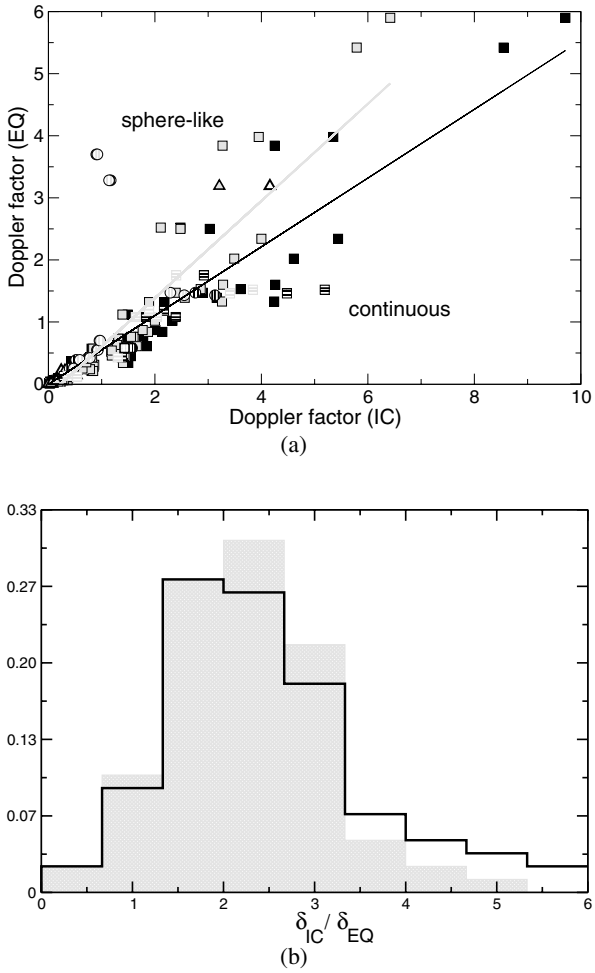

Fig. 9. The relation between the equipartition $\delta_{\rm EQ}$ and $\delta_{\rm IC}$ factor for spherical and continuous jets is shown in **a)**. The continuous-jet case is displayed in black symbols (same symbol forms as in Fig. 6). The solid lines represent linear regressions to the data (black: continuous jets, grey: spherical jets). In **b)** a histogram shows the ratio between $\delta_{\rm IC}$ and $\delta_{\rm EQ}$ for continuous jets (black) and spherical jets (grey).

Although we do not find any significant trend with regard to these two parameters, we include the calculated values for Γ and ϕ for completeness in Tables 3 and 4.

4.2.5. Brightness temperature

We observationally determine the brightness temperature via the following relation:

$$T_{\rm B} = 1.77 \times 10^{12} \frac{F_{\rm m}}{\theta_{\rm d}^2 \nu_{\rm m}^2}(1+z) \quad (7)$$

for continuous jets (taken from Ghisellini et al. 1993). The intrinsic brightness temperature can be determined from the observed one using the relation $T_{\rm B} = T_{\rm Bi}\delta$ for the case of the moving sphere or $T_{\rm B} \propto \delta^{(4-2\alpha)/(5-2\alpha)} T_{\rm Bi}$ for the continuous case. In Fig. 10 the distributions of the brightness temperatures (observed and intrinsic) for continuous jets are shown.

4.2.6. Core dominance parameter

Within the currently accepted scenario of relativistic beaming, the emission of AGN is composed of two components.

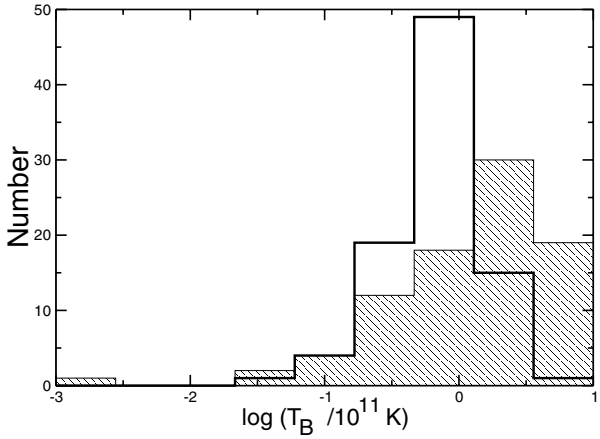

Fig. 10. The brightness temperature distribution for the observed brightness temperatures (solid line) and the intrinsic brightness temperatures (hatched area). In both cases the values for continuous jets have been determined.

The pc-scale emission arises from Doppler-boosted jet emission while the extended emission from mainly isotropic radiation. The ratio of the two emissions, in the sense compact/extended, is defined as the core dominance parameter (hereafter: R; e.g., Orr & Brown 1982). In the literature, R is either calculated as ratio of flux densities or as ratio of luminosities (e.g., Punsly 1995). R is defined here as the ratio of the flux densities. In both cases, R gives a measure for the role beaming plays in the appearance of this source. In Fig. 11 we show the R-distributions for the three optical classes of objects. We calculate and compare two core dominance parameters, both using the Green Bank 5 GHz flux density as the denominator: $R_{\rm V}$ uses the total VLBI flux density from Taylor et al. (1996), and $R_{\rm C}$ uses the VLBI core flux density taken from the model-fit parameters of Paper I. The value for R is expected to be smaller than 1 since the Green Bank flux contains the complete flux of the source while the "compact" portion only contains the flux from the central region of the source. The reason for calculating and comparing both values is that we expect to see an even clearer trend in using the VLBI core flux, although usually the total VLBI flux is used. Optically thin components contribute to the total VLBI flux while these components do not contribute to R calculated with the core flux only. In Table 8 we list the median values for the different types of objects and mark the different types of R. We find in general smaller median values for those R that have been calculated based on the VLBI core flux for all classes of objects. In addition $R_{\rm C}$ shows larger differences between the values for the individual classes. We find significantly higher values of $R_{\rm C}$ for the quasars compared to the radio galaxies (K-S test: 0.0001) and for the BL Lac objects compared to the radio galaxies (K-S test: 0.009) when considering all sources, detected by *ROSAT* or not. This finding also applies both for the detected sample (KS-Test Q/G: 0.032; B/G: 0.050) as for the non-detected subsample (Q/G: 0.006, B/G: 0.056). Fan & Zhang (2003) find smaller R for radio galaxies than for quasars, which are even smaller than for BL Lac objects. This is in agreement with our results presented here. The distributions of R for all the detected and non-detected objects per source class are shown in Fig. 12. We find no significant differences between the detected and non-detected subsamples of classes of objects. In Fig. 13 we show the relation between the logarithms of $\delta_{\rm IC}^{\rm con}$ and $R_{\rm C}$. A correlation coefficient of 0.28 is not significant.

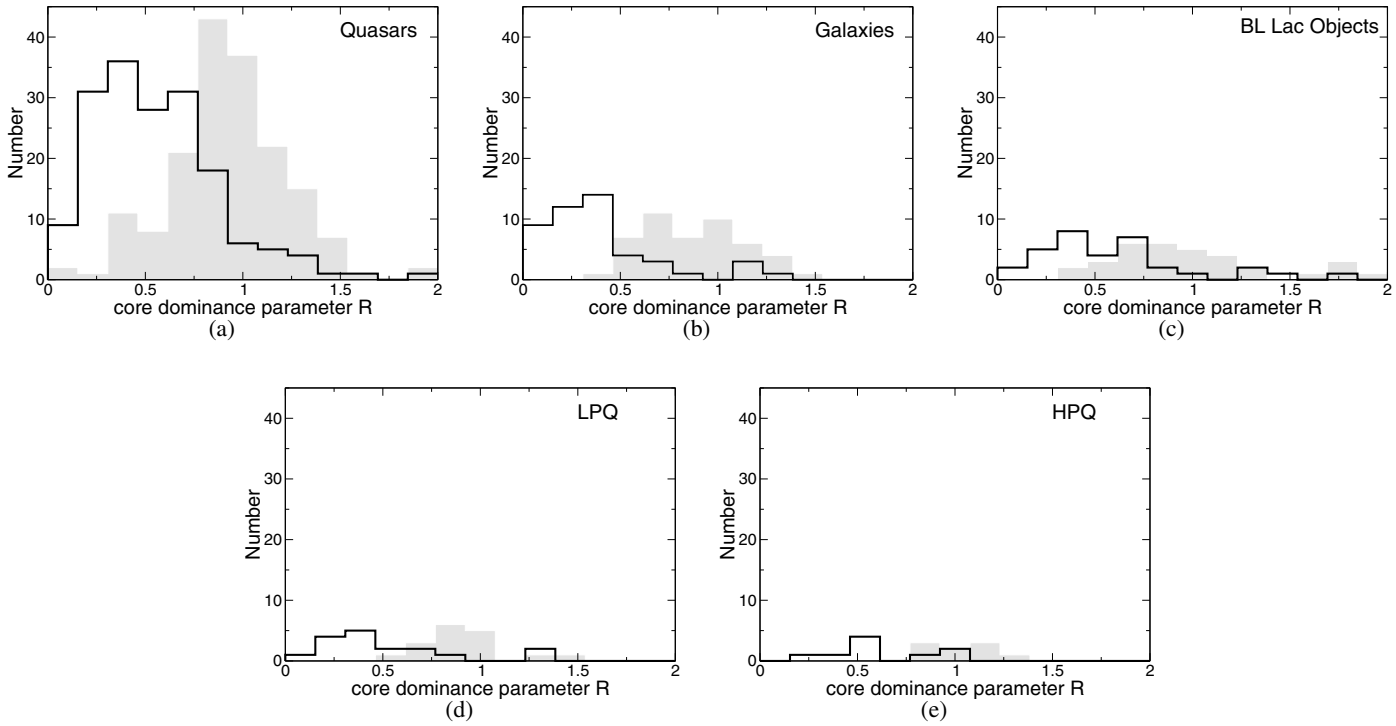

Fig. 11. The distribution of the core dominance parameter R is shown for different classes of objects. We show the distributions of R defined as ratio between the VLBI core flux-density (R_C, solid line) and the total VLBI flux-density (R_V, grey), and the Green Bank 5 GHz flux-density.

Table 8. Median values for the core dominance parameter R based on two sorts of VLBI flux-density measures and the Green Bank 5 GHz flux-densities. The Green Bank and total VLBI flux-densities have been taken from Taylor et al. (1996). For those sources where no total VLBI flux-densities were given in Taylor et al., we obtained the values from Paper I. The VLBI core flux-densities have been taken from Paper I.

	Sample	Q	G	B	LPQ	HPQ
R_C (VLBI core flux)	All	0.52	0.33	0.54	0.39	0.52
R_V (total VLBI flux)	All	0.92	0.84	0.90	0.90	1.06
R_C (VLBI core flux)	detections	0.50	0.35	0.54	0.38	0.53
R_C (VLBI core flux)	non-detections	0.54	0.33	0.56	0.48	0.52

4.2.7. Tabulated values

All values calculated in this and the following sections are listed in Tables 3−6 (these tables are only available in the online edition of the Journal). The values shown in the plots of this paper are listed in Table 3 (for the sources not detected by *ROSAT*), and in Table 4 (for the sources detected by *ROSAT*). Not all of the CJF sources could be included in the correlation analysis since β_{app} could not be determined for all the sources. A detailed overview of the sources and jet components that have been used for the kinematic analysis, and the reasons for source elimination from this kinematic analysis, is given in Paper II. For completeness we list in Tables 5 and 6 values for those sources without β_{app}. These values are not shown in the plots of this paper. Tables 3 and 4 list the source name (1) and β_{app} (2). Columns (3)−(9) list parameters obtained under the assumption of a uniform spectral index $\alpha = -0.75$: δ_{IC} (3), the continuous δ_{IC} (4), δ_{EQ} (5), the logarithm of the observed brightness temperature T_B (6), the logarithm of the intrinsic brightness temperature T_{Bi}^{con} (7), the bulk Lorentz factor Γ_{sl} (8), and the angle to the line of sight ϕ (9). Columns (10)−(16) list the same parameters computed using each source's observed spectral index (Taylor et al. 1996). Continuing, the remainder of the columns list the VLBI flux (17, taken from Taylor et al. 1996), the flux of the core determined from the model-fit parameters (18, taken from Paper I), the logarithm of the core dominance R_C calculated on the basis of the VLBI core flux-density (19), and the core dominance R_V calculated on the basis of the total VLBI flux-density (20). We used the 1-year WMAP data (Spergel et al. 2003) to obtain values for the cosmological parameters ($h = 0.71$, $\Omega_m h^2 = 0.135$, and $\Omega_{tot} = 1.02$); differences in the apparent velocities due to differences between the 1-year and 3-year WMAP parameters are negligible with respect to the formal measurement errors of the velocities. This is discussed in more detail in Paper II.

Tables 5 and 6 list the source name in Col. (1). Columns (2)−(6) list parameters obtained under the assumption of a uniform spectral index $\alpha = -0.75$: δ_{IC} (2), the continuous δ_{IC} (3), δ_{EQ} (4) the observed brightness temperature T_B (5), and the logarithm of the intrinsic brightness temperature T_{Bi}^{con} (6). Columns (7)−(11) list the same parameters computed using each source's observed spectral index. Continuing, the remainder of the columns list the VLBI flux (12, taken from Taylor et al. 1996), the flux of the core determined from the model-fit parameters (13, taken from Paper I), the logarithm of the core dominance R_C (14), and the core dominance R_V (15).

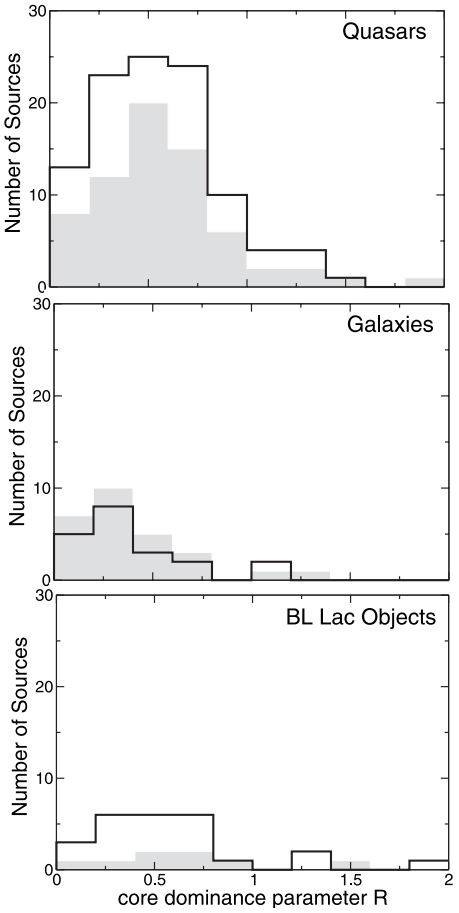

Fig. 12. The core dominance parameter R (based on the CJF core flux-density) is shown for the *ROSAT* detected objects and for the non-detections (grey) for the main three classes of objects.

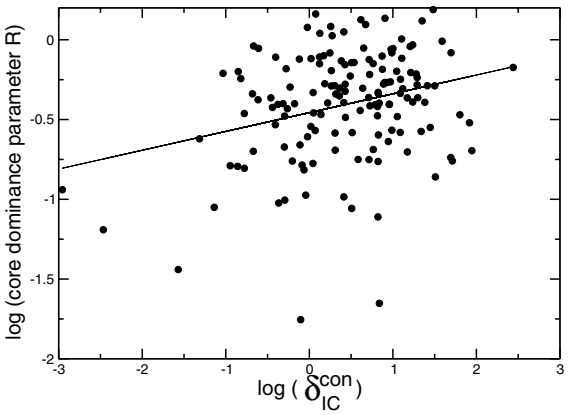

Fig. 13. The relation between the logarithms of $\delta_{\rm IC}^{\rm con}$ and the core dominance parameter $R_{\rm C}$ is shown.

4.3. kpc-scale morphologies of CJF-AGN and the misalignment between pc- and kpc-scale structure

4.3.1. Misalignment

Pearson & Readhead (1988) found in the distribution of position angle differences between pc- and kpc-scales (ΔPA) a highly unexpected bimodal pattern of relatively well aligned and roughly orthogonal jets. More current investigations of larger samples by, e.g., Conway & Murphy (1993) proved this excess to be statistically significant compared to the predictions of simple models. The so-called "misaligned population" of core-dominated AGN reveals a ΔPA of 70° to 90° (termed the "secondary peak" by Appl et al. 1996). The position angle distributions of large samples of AGN have been studied in detail by e.g., Pearson & Readhead 1988; Wehrle et al. 1992; Conway & Murphy 1993; Appl et al. 1996. In Fig. 14a we show the histogram of misalignment angle for a sample of 155 radio sources together with the best fit by simple bend models by Appl et al. (1996). A K-S test (0.016) suggests that it is unlikely for the misalignment data to have been drawn from a parent population represented by the maximum likelihood model.

Small apparent misalignments can be explained by small random bends. Small intrinsic bends between pc- and kpc-scales will give the large ΔPAs that are observed if sources are viewed almost along the direction of the VLBI jet. Assuming similar intrinsic bends, sources in which the VLBI jet is oriented closer to the line of sight should show more extreme misalignment angles. The orthogonal misalignments, however cannot be explained by these processes (Conway & Murphy 1993).

Several ΔPA-distributions of different AGN-samples have been published; however, no complete compilation of ΔPA values is currently available. We performed a literature search for kpc-scale morphological information on the CJF sources. In Table 1 (Col. 10) we describe the VLA structure of the sources. The major part of the information on the large scale structures has been derived by T. Pearson in VLA observations of the CJ-sources (`http://www.astro.caltech.edu/~tjp/cj/`). However, VLA maps were not available for all sources; this is indicated for such cases in the table. To build up a homogeneous database for this kind of analysis, we redetermined the orientation of the large-scale structures from published maps and compared them with the pc-scale orientation derived directly from the CJF VLBI survey results (Paper I). This sample is the largest homogeneous sample for this kind of misalignment study in AGN being so far available.

114 of the 293 CJF-sources reveal a point-like VLA structure and do not contribute to this analysis. In Fig. 14b we display the distribution of ΔPA for those CJF sources that reveal kpc-scale extended emission. The figure clearly shows the expected peak around 0° (and a smaller peak around 150°−180°) for the aligned objects and an indication for the secondary peak around 75° for the misaligned objects.

In Figs. 14c−e we show the ΔPA-distribution for the three classes of objects: quasars, BL Lac objects, and radio galaxies, respectively. The quasar distribution (c) contains more objects and is broader, covering the complete range of misalignment angles. Here we find some indication for the secondary peak. The radio galaxies (e) show primarily aligned kpc- and pc-scale jets: the distribution peaks around 0° and 180°, while no misaligned objects have been observed. A fraction of the BL Lac objects (d) seems to be misaligned.

In Fig. 15 we compare the distributions of the misalignment angle for the *ROSAT*-detected and non-detected sources. Based on a K-S test the distributions are not significantly different (0.260).

4.3.2. Investigating the relation between the large scale structure of AGN and X-ray emission

At least part of the X-ray emission from radio-loud AGN is thought to arise from the jet, because radio-loud objects have stronger X-ray emission and rather different X-ray spectra than do radio-quiet objects (e.g., Mushotzky 1993, and references

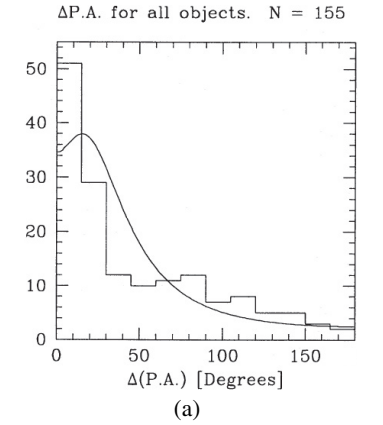

(a)

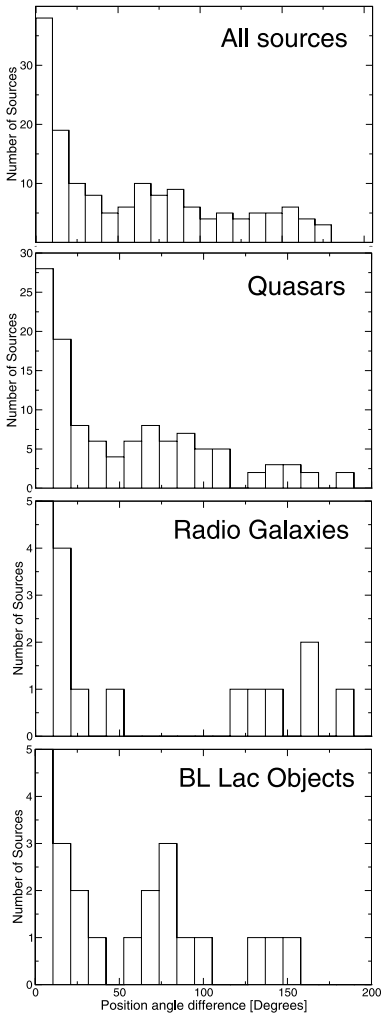

(b)

Fig. 14. The panels **a)**–**b)** show histograms of the misalignment distribution. Figure **a)** is taken from Appl et al. (1996) for a compilation of 155 sources. The superimposed smooth line shows the best fit by simple bend models performed by Appl et al. In **b)** we show for the complete CJF sample (all sources with VLA- and VLBI-information) the misalignment distribution for the three main classes of sources (quasars: 114 sources, radio galaxies: 17 sources, and BL Lac objects: 22).

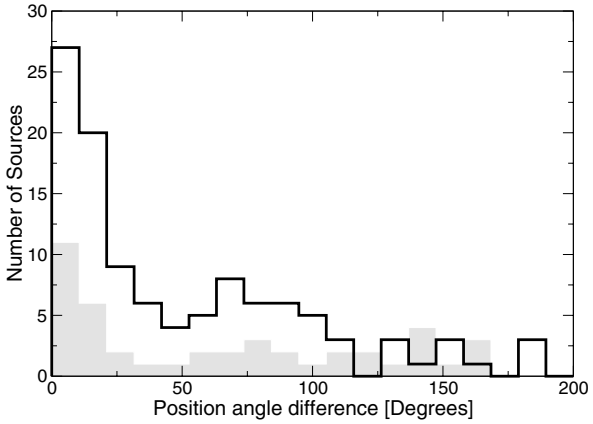

Fig. 15. The distribution of the misalignment angle for the *ROSAT*-detected (solid line) and non-detected (grey) subsample.

therein). Surveys of extended radio jets with *CHANDRA* yield evidence that the X-ray emission is related to the kpc-scale morphology (e.g., Sambruna et al. 2004; Gelbord et al. 2004). In this section we therefore contrast the kpc-scale radio morphology of the *ROSAT* detected and non-detected objects to search for signs of this assumed correlation.

114 of the 293 CJF-sources reveal a point-like VLA structure. Among those, 65 have not been detected by *ROSAT*, but 49 have been detected. Except for two objects (0014+813, 1246+586), the point-like sources have relatively low X-ray fluxes. We find significant evidence that *ROSAT*-detected sources tend to show extended radio emission on large scales. In order to be able to classify the extended morphology of the CJF kpc-scale jets, we adopted a classification scenario. The large-scale structures appear to be either unresolved, slightly resolved, jet-like and extended, double, or more complex. Sometimes complex jet- and counter-jets are visible in the large-scale maps; halo emission can appear along with jets or be the only large-scale component.

To quantify the large-scale structure, we adopted complexity-factors, where the number increases with the complexity of the morphology: the unresolved sources were classified as **0**, the slightly resolved sources as **1**, sources with a clearly resolved jet as **2**, double-source morphologies as **3**, jet-counter-jet structures as **4**, and the most complex morphologies as **5**. Examples for the differently complex structures and the assignment of the complexity-factors are shown in Fig. 16.

In Table 9 we list the distribution of these complexity-factors for the detected CJF sources and the non-detections. There are significant differences between the two distributions: the non-detected objects tend to show less complex kpc-scale structure, while the *ROSAT* detected CJF sources tend to have more complex kpc-scale structures. A K-S test (0.005) comparing the binned detected and non-detected complexity factors allows us to reject strongly the hypothesis that these two distributions are the same. Sources with the most complex large-scale structures (**4**, **5**) are almost always (∼97%) detected by *ROSAT*. However, there may be a redshift-dependent effect at work here. The average redshift of *ROSAT*-detected sources that have the most complex large-scale radio morphologies is 0.67, whereas for all sources detected by *ROSAT* it is 1.20, and for non-*ROSAT*-detected sources it is 1.34.

The large-scale jet structure might play an important role in contributing to the X-ray emission. Jets are very likely relativistic on kiloparsec scales as well. Large-scale relativistic proper motions have been directly observed in the nearby Radio Galaxy M87 (Biretta & Junor 1995). The most plausible explanation of some of the newly discovered extended X-ray jets

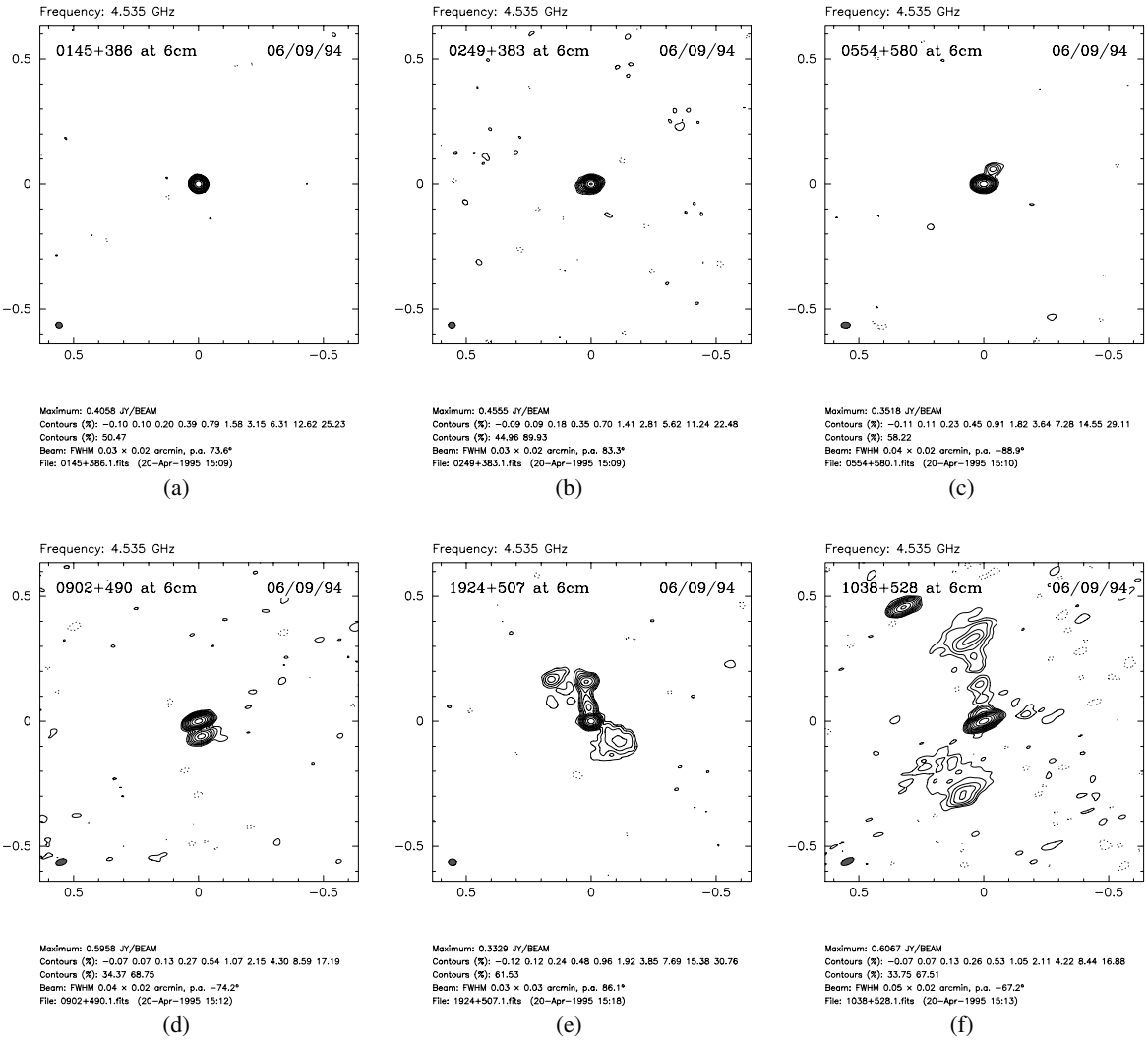

Fig. 16. Six maps (images have been taken from `http://www.astro.caltech.edu/~tjp/cj/`) showing examples for the structures described by the complexity-factor (from **a)**–**f)** and **0** to **5**, respectively).

Table 9. The numbers of objects with the complexity-factors describing the kpc-scale structure.

complexity factor	**0**	**1**	**2**	**3**	**4**	**5**
detected by *ROSAT*	49	12	35	27	20	15
not detected by *ROSAT*	65	10	32	11	1	0

requires that the plasma have bulk relativistic motions on scales of hundreds of kiloparsecs (e.g., Tavecchio et al. 2000; Celotti et al. 2001; Sambruna et al. 2002). More observations are definitely required to search for and confirm large scale motion in these *ROSAT* detected quasars and BL Lac objects.

5. Discussion

Although AGN form the ideal class of objects for multi-wavelength studies – as their emission can cover almost 20 orders of magnitude in frequency from the radio to the γ-ray band – our knowledge about their physics is limited by observational constraints and the inherent complex physical processes. Studies with multifrequency coverage for a single object are rare (e.g., NGC 3783, 3C 273, 3C 279). While *CHANDRA* observations determined the X-ray production mechanisms in a growing number of AGN (e.g., Harris & Krawczynski 2002), this information is not available for a substantial number of sources in any large survey such as the CJF. However, assuming that the dominant mechanism is IC emission, we can place lower limits on beaming parameters derived from *ROSAT* observations for the complete CJF. To date this kind of analysis has relied on smaller samples and/or data taken from the literature. With the *ROSAT* observations of a complete and homogeneous VLBI survey, beaming indicators relying on radio and X-ray data can be estimated on an improved statistical basis. We draw the following conclusions:

- More than half of the CJF sources have been detected by *ROSAT*. The good correlation between the radio- and X-ray luminosities of the CJF sources on the one hand and between the optical- and the X-ray luminosities on the other hand support the explanation that a common origin of the radiation can be derived, whereas differences exist between radio galaxies and quasars, beyond their different luminosities, which might be explained by an additional cluster emission in the case of the radio galaxies.
- We find higher apparent velocities for the *ROSAT*-detected and non-detected quasars compared to the radio galaxies.

Radio galaxies reveal the lowest values in both subsamples. We find some evidence for different apparent velocity distributions between those quasars detected by *ROSAT* and those not detected. A statistically significant analysis of the apparent motions of the BL Lac objects is hampered by small numbers of objects.

– The calculation of the Doppler factors making use of the observationally determined spectral indices leads to different distributions compared to the calculations based on a uniform spectral index.
We find a better match between the median $\beta_{\rm app}$ and both $\delta_{\rm IC}$ calculated with the observed spectral indices compared to the uniformly assumed spectral index for all classes of objects. The comparison of the IC Doppler factor with $\beta_{\rm app}$ (for those sources detected by *ROSAT*) seems to indicate that the bulk relativistic motion without any additional pattern speeds can explain the observations for quasars and BL Lac objects. However, larger source numbers (especially for the BL Lac objects) would be beneficial. The quasars have significantly larger values of $\delta_{\rm IC}^{\rm sp}$ and $\delta_{\rm IC}^{\rm con}$ compared to radio galaxies.
– We find a good agreement between the Doppler factors derived from equipartition arguments and from IC calculations, especially in the case of a continuous jet model. $\delta_{\rm IC}$ is about 2−2.5 times $\delta_{\rm EQ}$ in the case of the continuous and the sphere-like jet case.
– By investigating the distribution of the core dominance parameter R calculated on the one hand by the ratio between the total VLBI flux-density at 5 GHz and the Green Bank 5 GHz flux-density, and on the other hand by the ratio between the VLBI core flux-density and the Green Bank flux-density, we find that the latter is better suited to discriminate between differently beamed objects. We find evidence for stronger beaming in quasars and BL Lac objects compared to the radio galaxies for all samples investigated. Within the individual classes, we find no significant differences between the *ROSAT*-detected and non-detected subsamples.
– Pronounced extended radio structure is detected for most of the CJF sources. Roughly only one-third of the sources are strongly core-dominated and do not reveal kpc-scale structure. Misalignments between the preferential direction on pc-scales and the direction of the overall structure have been found to be more common than expected in "simple" beaming models for some investigated AGN samples by e.g., Conway & Murphy (1993) and Appl et al. (1996). Whereas radio galaxies do not show misaligned sources in our CJF sample, quasars and BL Lac objects show this effect. This can be explained by amplification of small intrinsic bends due to projection effects (e.g., Conway & Murphy 1993; Conway & Wrobel 1995).
– 114 out of 293 sources from the complete CJF show no extended radio emission. For these objects the probability of *ROSAT* detectable X-ray emission is significantly lower than for the whole sample. There exist clear correlations between the extended radio structure and the likelihood of *ROSAT* detection. Sources detected by *ROSAT* show a higher degree in the complexity of their large-scale radio morphologies. However, we cannot exclude that a redshift-dependent effect influences this relation. The average redshift of *ROSAT*-detected sources with most complex large-scale radio structure is 0.67 compared to 1.20 for all sources detected by *ROSAT*.

Acknowledgements. We wish to thank A. Witzel and T. P. Krichbaum for thought-provoking discussions and many useful comments. The *ROSAT* project is supported by the Bundesministerium für Bildung, Wissenschaft, Forschung und Technologie (BMBF) and the Max-Planck-Gesellschaft. Part of this work was supported by the European Commission, TMR Programme, Research Network Contract ERBFMRXCT97-0034 CERES and by the DLR, project 50QD0101. S. Britzen acknowledges support by the Claussen-Simon Stiftung. This research has made use of the NASA/IPAC Extragalactic Data Base (NED) which is operated by the Jet Propulsion Laboratory, California Institute of Technology, under contract with the National Aeronautics and Space Administration.

References

Antonucci, R. R. J. 1986, ApJ, 304, 634
Antonucci, R. R. J., & Ulvestad, J. S. 1985, ApJ, 294, 158
Appl, S., Sol, H., & Vicente, L. 1996, A&A, 310, 419
Barthel, P. D. 1989, ApJ, 336, 606
Barthel, P. D., Pearson, T. J., Readhead, A. C. S., & Canzian, B. J. 1986, ApJ, 310, L7
Baum, S. A., O'Dea, C. P., Murphy, D. W., & de Bruyn, A. G. 1990, A&A, 232, 19
Biretta, J. A., & Junor, W. 1995, Proc. Natl. Acad. Sci. USA, 92, 11364
Biretta, J. A., Stern, C. P., & Harris, D. E. 1991, AJ, 101, 1632
Bridle, A. H., & Fomalont, E. B. 1978, AJ, 83, 704
Brinkmann, W., Siebert, J., & Boller, Th. 1994, A&A, 281, 355
Brinkmann, W., Yuan, W., & Siebert, J. 1997, A&A, 319, 413
Brinkmann, W., Wang, T., Matsuoka, M., & Yuan, W. 1999, A&A, 345, 43
Brinkmann, W., Grupe, D., Branduardi-Raymont, G., & Ferrero, E. 2003, A&A, 398, 81
Britzen, S. 2002, Rev. Mod. Astron., 15, 199
Britzen, S., Vermeulen, R. C., Taylor, G. B., et al. 2001, in High Energy Gamma-Ray Astronomy, ed. F. A. Aharonian, & H. J. Völk, AIP Proc., 558, 721
Britzen, S., Vermeulen, R. C., Taylor, G. B., et al. 2007a, A&A, 472, 763 (Paper I)
Britzen, S., Vermeulen, R. C., Campbell, R. M., et al. 2007b, A&A, submitted, (Paper II)
Browne, I. W. A., & Perley, R. A. 1986, MNRAS, 222, 149
Browne, I. W. A., & Murphy, D. W. 1987, MNRAS, 226, 601
Browne, I. W. A., Wilkinson, P. N., Patnaik, A. R., & Wrobel, J. M. 1998, MNRAS, 293, 257
Cassaro, P., Stanghellini, C., Bondi, M., et al. 1999, A&AS, 139, 601
Celotti, A., Ghisellini, G., & Chiaberge, M. 2001, MNRAS, 321, L1
Cohen, & Vermeulen 1992
Conway, J. E., & Murphy, D. W. 1993, ApJ, 411, 89
Cruddace, R. G., Hasinger, G. R., & Schmitt, J. H. 1988, in Proc. of the Workshop: Astronomy from large data bases, ed. F. Murtagh, & A. Heck, ESO Conf. Proc., 28, 177
Dickey, J. M., & Lockman, F. J. 1990, ARA&A, 28, 215
Eckart, A., Hummel, C. A., & Witzel, A. 1989, MNRAS, 239, 381
Fan, J. H., & Zhang, J. S. 2003, A&A, 407, 899
Garrington, S. T., Conway, R. G., & Leahy, J. P. 1991, MNRAS, 250, 171
Gelbord, J. M., Marshall, H. L., Schwartz, D. A., et al. 2004, Proceedings of X-Ray and Radio Connections, ed. L. O. Sjouwerman, & K. K Dyer, published electronically by NRAO, `http://www.aoc.nrao.edu/events/xraydio`, Santa Fe, New Mexico, USA
Ghisellini, G. 1987, Ph.D. Thesis, SISSA, Trieste
Ghisellini, G., Padovani, P., Celotti, A., & Maraschi, L. 1993, ApJ, 407, 75
Giovannini, G., Taylor, G. B., Arbizzani, E., et al. 1999, ApJ, 522, 101
Gregory, P. C., & Condon, J. J. 1991, ApJS, 75, 1011
Güijosa, A., & Daly, R. A. 1996, ApJ, 461, 600
Harris, D. E., & Krawczynski, H. 2002, ApJ, 565, 244
Harris, D. E., Leighly, K. M., & Leahy, J. P. 1998, ApJ, 499, 149
Henstock, D. R., Browne, I. W. A., Wilkinson, P. N., et al. 1995, ApJS, 100, 1
Hummel, C. A., Krichbaum, T. P., Witzel, A., et al. 1997, A&A, 324, 857
Johnston, K. J., Biermann, P., Eckart, A., et al. 1984, ApJ, 280, 542
Jones, T. W., O'Dell, S. L., & Stein, W. A. 1974, ApJ, 428, 130
Kim, K.-T., Kronberg, P. P., & Tribble, P. C. 1991, ApJ, 379, 80
Königl, A. 1981, ApJ, 243, 700
Kühr, H., Witzel, A., Pauliny-Toth, I. I. K., & Nauber, U. 1981, A&AS, 45, 367
Kühr, H., Stocke, J. T., Strittmatter, P. A., et al. 1986, ApJ, 302, 52
Lind, K. R., & Blandford, R. D. 1985, ApJ, 295, 358
Machalski, J. 1998, A&AS, 128, 153
Machalski, J., & Condon, J. J. 1983, AJ, 88, 143
Machalski, J., & Brandt, W. N. 1996, MNRAS, 282, 1305
Machalski, J., Maslowski, J., Condon, J. J., & Condon, M. A. 1982, AJ, 87, 1150
Marcha, M. J. M., Browne, I. W. A., Impey, C. D., & Smith, P. S. 1996, MNRAS, 281, 425
Marscher, A. P. 1977, ApJ, 216, 244

Marscher, A. P. 1980, ApJ, 235, 386
Marscher, A. P. 1987, in Superluminal Radio Sources, ed. A. Zensus, & T. J. Pearson (Cambridge: Cambridge Univ. Press), 280
Murphy, D. W., Browne, I. W. A., & Perley, R. A. 1993, MNRAS, 264, 298
Mushotzky, R. F. 1993, ARA&A, 31, 717
Myers, S. T., Jackson, N. J., Browne, I. W. A., et al. 2003, MNRAS, 341, 1
Neff, S. G., & Hutchings, J. B. 1990, AJ, 100, 1441
Orr, M. J. L., & Browne, I. W. A. 1982, MNRAS, 200, 1067
Owen, F. N., & Puschell, J. J. 1984, AJ, 89, 932
Padovani, P., & Giommi, P. 1995, ApJ, 444, 567
Patnaik, A. R., Browne, I. W. A., Wilkinson, P. N., & Wrobel, J. M. 1992, MNRAS, 254, 655
Patnaik, A. R., Browne, E. W. A., King, L. J., et al. 1993, MNRAS, 261, 435
Peacock, J. A., & Wall, J. V. 1982, MNRAS, 198, 843
Pearson, T. (http://www.astro.caltech.edu/~tjp/cj/)
Pearson, T. J., & Readhead, A. C. S. 1988, ApJ, 328, 114
Pedlar, A., Booler, R. V., & Davies, R. D. 1983, MNRAS, 203, 667
Pedlar, A., Ghataure, H. S., Davies, R. D., et al. 1990, MNRAS, 246, 477
Perley, R. A. 1982, AJ, 87, 859
Perley, R. A., Fomalont, E. B., & Johnston, K. J. 1982, ApJ, 255, 93
Pfeffermann, E., Briel, U. G., Hippmann, H., et al. 1986, Proc. SPIE, 733, 519
Polatidis, A. G., Wilkinson, P. N., Xu, W., et al. 1995, ApJS, 98, 1
Price, R., Gower, A. C., Hutchings, J. B., et al. 1993, ApJS, 86, 365
Punsly, B. 1995, AJ, 109, 4, 1555
Readhead, A. C. S. 1993, in Sub-Arcsecond Radio Astronomy, ed. R. J. Davis, & R. S. Booth (Cambridge: Cambridge Univ. Press), 173
Readhead, A. C. S. 1994, ApJ, 426, 51
Reid, A., Shone, D. L., Akujor, C. E., et al. 1995, A&AS, 110, 213
Sambruna, R. M., Maraschi, L., Tavecchio, F., et al. 2002, ApJ, 571, 206
Sambruna, R. M., Gambill, J. K., Maraschi, L., et al. 2004, ApJ, 608, 698
Scott, M. A., & Readhead, A. C. S. 1977, MNRAS, 215, 383
Slee, O. B., & Siegman, B. C. 1983, PASAu, 5, 114
Spergel, D. N., Verde, L., Peiris, H. V., et al. 2003, ApJS, 148, 175
Stark, A. A., Gammie, C. F., & Wilson, R. W. 1992, ApJS, 79, 77
Tavecchio, F., Maraschi, L., Sambruna, R. M., & Urry, C. M. 2000, ApJ, 544, L23
Taylor, G. B., Vermeulen, R. C., Pearson, et al. 1994, ApJS, 95, 345
Taylor, G. B., Vermeulen, R. C., Readhead, A. C. S., et al. 1996, ApJS, 107, 37
Thakkar, D. D., Xu, W., Readhead, A. C. S., et al. 1995, ApJS, 98, 33
Thean, A., Pedlar, A., Kukula, M. J., et al. 1999, MNRAS, 314, 573
Trümper, J. 1983, Adv. Space Res., 2, 241
Ulvestad, J. S. 1985, ApJ, 288, 514
Ulvestad, J. S., Johnston, K. J., & Weiler, K. W. 1983, ApJ, 266, 18
Urry, C. M., & Padovani, P. 1995, PASP, 107, 803
Véron-Cetty, M.-P., & Véron, P. 2001, A&A, 374, 92
Vigotti, M., Grueff, G., Perley, R., et al. 1989, AJ, 98, 419
Voges, W., Aschenbach, B. Boller, Th., et al. 2000, IAU Circ, 7432, 3
Wagner, S. J., Witzel, A., & Heidt, J. 1996, AJ, 111, 2187
Wehrle, A. E., Cohen, M. H., Unwin, S. C., et al. 1992, ApJ, 391, 589
White, R. L., & Becker, R. H. 1992, ApJS, 79, 331
Wilkinson, P. N., Browne, I. W. A., Patnaik, A. R., et al. 1998, MNRAS, 300, 790
Witzel, A., Schalinski, C. J., Biermann, P. L., et al. 1988, A&A, 206, 245
Xu, W., Readhead, A. C. S., Pearson, T. J., et al. 1995, ApJS, 99, 297
Zensus, J. A., & Pearson, T. J. 1987, Superluminal radio sources (Cambridge and New York: Cambridge University Press)
Zimmermann, H. U., Becker, W., Belloni, T., et al. 1994, MPE Rep., 257

Online Material

Table 3. Calculated values for those sources that have not been detected by *ROSAT*.

		$\alpha = -0.75$							observed α										
Source	$\beta_{\rm app}$	$\delta_{\rm IC}$	$\delta_{\rm IC}^{\rm con}$	$\delta_{\rm EQ}$	log $(T_{\rm B}/10^{11})$	log $(T_{\rm Bi}^{\rm con}/10^{11})$	$\Gamma_{\rm sl}$	ϕ	$\delta_{\rm IC}$	$\delta_{\rm IC}^{\rm con}$	$\delta_{\rm EQ}$	log $(T_{\rm B}/10^{11})$	log $(T_{\rm Bi}^{\rm con}/10^{11})$	$\Gamma_{\rm sl}$	ϕ	VLBI flux	VLBI core flux	log $(R_{\rm C})$	$R_{\rm V}$
	[c]				[K]	[K]		[deg]				[K]	[K]		[deg]	[mJy]	[mJy]		
(1)	(2)	(3)	(4)	(5)	(6)	(7)	(8)	(9)	(10)	(11)	(12)	(13)	(14)	(15)	(16)	(17)	(18)	(19)	(20)
0016+731	5.893	0.12	0.07	0.02	–0.93	–0.14		7.20	0.15	0.09	0.00	–0.93	–0.23	860.16	7.20	1056	1673	–0.21	0.98
0108+388	0.460	0.27	0.21	0.05	–0.62	–0.15	2.35	–52.22	0.23	0.17	0.01	–0.62	–0.07	2.79	–51.29	456	1714	–0.46	1.30
0133+476	3.287	4.78	6.77	2.41	0.85	0.28	3.63	11.37	9.07	17.26	0.80	0.85	0.07	5.18	4.09	1686	1795	–0.03	0.99
0227+403	3.531	0.34	0.27	0.10	–0.40	0.00	19.73	31.36	1.04	1.05	0.01	–0.40	–0.41	7.01	29.38	332	550	–0.12	1.26
0444+634	10.927	2.60	3.22	1.56	0.66	0.30	24.44	9.90	3.72	5.27	0.58	0.66	0.18	18.03	9.38	368	654	–0.22	1.08
0554+580	1.124	0.19	0.13	0.04	–0.74	–0.13	6.00	82.40	0.20	0.14	0.01	–0.74	–0.15	5.78	82.32	146	293	–0.79	0.32
0627+532	10.199	1.85	2.12	1.38	0.59	0.37	29.27	10.85	10.84	32.34	0.15	0.59	–0.19	10.26	5.28	67	485	–0.86	1.00
0641+393	7.066	3.42	4.49	1.53	0.66	0.21	9.16	13.13	7.09	12.73	0.39	0.66	–0.03	7.14	8.11	458	577	0.01	1.27
0642+449	9.845	9.98	16.64	4.47	1.12	0.27	9.90	5.75	12.20	22.39	2.12	1.12	0.21	10.11	4.60	1568	1652	0.12	1.39
0646+600	0.192	1.49	1.62	0.55	0.25	0.10	1.09	17.11	1.76	2.01	0.20	0.25	0.04	1.17	10.23	475	1055	–0.29	1.15
0651+410	0.054	0.18	0.13	0.07	–0.67	–0.05	2.80	–6.40	0.33	0.24	0.01	–0.67	–0.28	1.68	–6.94	179	341	–0.38	0.80
0711+356	3.015	2.74	3.43	1.93	0.72	0.35	3.21	21.13	15.37	51.48	0.26	0.72	–0.19	8.01	1.41	157	1245	–0.76	1.38
0714+457	2.920	2.83	3.57	2.05	0.73	0.35	3.10	20.57	5.70	9.72	0.58	0.73	0.12	3.69	8.31	397	524	–0.08	1.09
0724+571	4.588	1.04	1.05	0.48	0.17	0.16	11.09	23.46	3.07	4.49	0.08	0.17	–0.21	5.13	17.31	349	556	–0.05	1.42
0800+618	7.941	9.86	16.40	5.59	1.19	0.34	8.18	5.69	17.25	38.75	2.01	1.19	0.17	10.48	2.53	961	1187	–0.01	1.21
0900+520	9.389	0.10	0.06	0.01	–1.13	–0.27	465.40	12.16	0.23	0.15	0.00	–1.13	–0.62	190.77	12.15	225	302	–0.24	0.77
0930+493	13.929	0.16	0.11	0.03	–0.87	–0.21	597.27	8.21	0.93	0.90	0.00	–0.87	–0.85	105.34	8.18	61	559	–0.97	0.97
0942+468	1.513	0.10	0.06	0.02	–1.06	–0.21	16.72	66.77	0.22	0.14	0.00	–1.06	–0.53	7.59	66.15	224	353	–0.20	1.00
0949+354	6.103	2.87	3.63	1.32	0.61	0.22	8.10	15.35	6.31	11.11	0.28	0.61	–0.04	6.19	9.12	256	374	–0.20	0.93
0950+748	0.515	0.23	0.16	0.03	–0.80	–0.25	2.91	–56.43	2.63	4.06	0.00	–0.80	–1.12	1.56	9.43	266	662	–0.44	0.90
1030+398	1.241	0.33	0.26	0.05	–0.59	–0.18	4.05	75.39	0.50	0.42	0.01	–0.59	–0.34	2.78	72.30	254	692	–0.41	1.07
1030+415	4.186	1.33	1.42	0.56	0.26	0.16	7.62	24.59	9.51	25.88	0.05	0.26	–0.48	5.73	4.48	250	390	–0.29	0.80
1031+567	0.472	0.27	0.20	0.05	–0.68	–0.20	2.41	–53.26	2.30	3.26	0.00	–0.68	–0.96	1.42	11.83	314	1090	–0.58	0.91
1106+380	3.320	0.27	0.20	0.08	–0.49	–0.01	22.27	33.33	2.24	3.22	0.00	–0.49	–0.76	3.80	23.83	76	681	–1.06	0.79
1124+571	8.056	0.93	0.91	0.22	–0.04	–0.02	36.02	13.97	5.01	9.36	0.02	–0.04	–0.59	9.08	10.26	325	424	–0.26	0.71
1143+590	6.965	1.38	1.48	0.57	0.31	0.19	18.68	15.75	1.42	1.53	0.20	0.31	0.18	18.18	15.71	357	581	–0.28	0.86
1144+542	3.426	1.99	2.32	0.80	0.41	0.16	4.20	25.00	4.38	6.87	0.14	0.41	–0.11	3.64	12.89	194	387	–0.40	0.80
1146+596	0.155	0.00	0.00	0.00	–2.80	–0.60	200.13	–17.62	0.00	0.00	0.00	–2.80	–0.88	107.42	–17.62	72	501	–0.94	0.80
1151+408	4.392	0.07	0.04	0.01	–1.26	–0.29	142.53	25.65	1.21	1.33	0.00	–1.26	–1.32	9.00	23.98	269	546	–0.15	1.44
1155+486	9.743	2.95	3.75	1.49	0.66	0.26	17.75	10.75	9.05	19.53	0.25	0.66	–0.10	9.82	6.32	258	351	–0.24	0.79
1216+487	6.684	1.87	2.14	0.63	0.33	0.10	13.17	15.83	8.72	19.90	0.08	0.33	–0.41	6.98	6.37	295	618	–0.36	0.91
1223+395	0.144	0.36	0.29	0.09	–0.44	–0.06	1.60	–18.71	1.70	2.07	0.01	–0.44	–0.62	1.15	8.57	200	506	–0.34	1.16
1321+410	0.297	0.11	0.07	0.02	–1.08	–0.28	4.95	–33.44	0.30	0.21	0.00	–1.08	–0.66	1.95	–35.90	189	413	–0.34	1.00
1323+800	13.881	2.56	3.16	1.12	0.55	0.20	39.10	7.97	4.88	7.74	0.25	0.55	–0.01	22.27	7.34	242	543	–0.28	1.19
1325+436	4.676	1.28	1.36	0.51	0.24	0.15	9.54	22.56	6.04	12.22	0.05	0.24	–0.37	4.91	9.26	140	595	–0.58	1.12
1337+637	8.546	0.29	0.22	0.04	–0.69	–0.24	126.92	13.33	1.45	1.66	0.00	–0.69	–0.82	26.23	12.98	173	389	–0.40	0.90
1356+478	0.146			0.01	–1.18			0.00			0.00	–1.18			0.00	237	446	–0.26	1.04
1424+366	4.670	1.02	1.02	0.25	–0.02	–0.02	11.72	23.15	1.15	1.19	0.07	–0.02	–0.07	10.46	22.87	623	759	0.16	1.77
1438+385	2.566	1.03	1.03	0.21	–0.08	–0.08	4.21	37.71	4.11	6.73	0.02	–0.08	–0.56	2.98	12.86	239	582	–0.60	0.62
1448+762	4.475	0.31	0.24	0.05	–0.62	–0.19	34.17	25.08	0.57	0.48	0.01	–0.62	–0.42	18.85	24.83	272	406	–0.40	0.59
1456+375	2.920	0.67	0.61	0.20	–0.19	–0.04	7.45	36.22	0.96	0.95	0.04	–0.19	–0.18	5.45	34.66	705	782	0.08	1.32
1459+480	0.771	0.71	0.65	0.22	–0.08	0.05	1.48	86.55	1.55	1.77	0.03	–0.08	–0.23	1.29	37.74	405	526	–0.08	1.08
1504+377	10.547	1.34	1.43	0.37	0.12	0.01	42.44	10.66	5.90	11.31	0.05	0.12	–0.48	12.46	8.27	331	685	–0.48	0.68
1543+480	2.265	0.40	0.33	0.08	–0.47	–0.14	7.89	46.56	3.43	5.80	0.00	–0.47	–0.89	2.61	15.93	313	494	–0.15	1.12
1732+389	5.104	11.64	20.08	8.36	1.29	0.38	6.98	3.64	54.51	275.95	2.21	1.29	–0.06	27.50	0.20	377	1228	–0.17	2.19
1734+508	1.102	0.59	0.52	0.13	–0.28	–0.08	2.17	75.71	1.71	2.04	0.01	–0.28	–0.47	1.50	34.95	162	828	–0.69	1.04
1812+412	6.689	0.95	0.94	0.30	0.05	0.06	24.61	16.68	3.99	6.65	0.03	0.05	–0.43	7.73	12.64	250	331	–0.33	0.62
1826+796	0.685	0.06	0.03	0.01	–1.45	–0.38	13.33	–68.93	0.09	0.05	0.00	–1.45	–0.58	8.12	–69.12	138	597	–0.62	1.03
1843+356	0.000	0.14	0.09	0.02	–0.97	–0.24	3.73	0.00	0.83	0.77	0.00	–0.97	–0.90	1.02	0.00	174	842	–0.66	1.06
1850+402	4.390	0.36	0.29	0.06	–0.53	–0.15	28.42	25.51	1.27	1.38	0.00	–0.53	–0.61	8.60	23.82	182	657	–0.47	1.23
1910+375	1.476	0.45	0.38	0.14	–0.27	0.02	3.74	64.90	2.05	2.69	0.01	–0.27	–0.52	1.80	28.78	191	374	–0.32	0.93
1943+546	0.183	0.01	0.00	0.00	–2.30	–0.43	83.79	–20.74	0.09	0.03	0.00	–2.30	–1.50	6.01	–20.89	34	967	–1.44	1.03
2007+659	0.645	5.47	7.98	3.88	0.99	0.37	2.86	2.52	23.40	82.48	0.78	0.99	–0.07	11.73	0.14	228	526	–0.52	0.70
2021+614	0.318	0.91	0.89	0.29	–0.01	0.03	1.06	–83.97	1.90	2.30	0.05	–0.01	–0.23	1.24	13.19	1219	2171	–0.35	0.79
2136+824	4.464	1.87	2.15	1.29	0.57	0.34	6.53	21.71	13.79	49.29	0.12	0.57	–0.29	7.65	2.44	93	285	–0.74	0.56
2235+731	3.389	0.37	0.30	0.10	–0.35	0.01	17.12	32.54	0.66	0.59	0.01	–0.35	–0.21	9.75	31.82	214	319	–0.30	0.75
2255+416	1.735	0.75	0.71	0.26	0.00	0.10	3.04	53.38	6.36	14.95	0.02	0.00	–0.61	3.50	4.67	220	1132	–0.70	1.02
2310+385	4.459	0.06	0.03	0.01	–1.34	–0.32	165.62	25.28	0.52	0.39	0.00	–1.34	–1.12	20.51	24.97	142	511	–0.53	1.06
2319+444	7.690	2.28	2.73	0.96	0.48	0.17	14.35	13.65	4.95	8.05	0.21	0.48	–0.09	8.55	10.54	499	552	0.14	1.51
2351+456	9.380	1.31	1.40	0.38	0.17	0.07	34.52	11.94	10.92	31.74	0.03	0.17	–0.62	9.53	5.20	589	791	–0.29	0.69
2352+495	0.362	0.01	0.01	0.00	–2.07	–0.52	38.59	–39.81	0.16	0.07	0.00	–2.07	–1.45	3.62	–40.64	138	1088	–1.05	0.70

Table 4. Calculated values for those sources that have been detected by *ROSAT*.

		$\alpha = -0.75$							observed α										
Source	$\beta_{\rm app}$	$\delta_{\rm IC}$	$\delta_{\rm IC}^{\rm con}$	$\delta_{\rm EQ}$	log $(T_{\rm B}/10^{11})$	log $(T_{\rm Bi}^{\rm con}/10^{11})$	$\Gamma_{\rm sl}$	ϕ	$\delta_{\rm IC}$	$\delta_{\rm IC}^{\rm con}$	$\delta_{\rm EQ}$	log $(T_{\rm B}/10^{11})$	log $(T_{\rm Bi}^{\rm con}/10^{11})$	$\Gamma_{\rm sl}$	ϕ	VLBI flux	VLBI core flux	log $(R_{\rm C})$	$R_{\rm V}$
	[c]				[K]	[K]		[deg]				[K]	[K]		[deg]	[mJy]	[mJy]		
(1)	(2)	(3)	(4)	(5)	(6)	(7)	(8)	(9)	(10)	(11)	(12)	(13)	(14)	(15)	(16)	(17)	(18)	(19)	(20)
0014+813	0.431	3.49	4.61	2.02	0.81	0.35	1.92	4.33	12.02	30.41	0.30	0.81	–0.04	6.06	0.34	851	1093	0.19	1.98
0035+413	5.430	6.42	9.71	5.90	1.16	0.47	5.58	8.85	6.43	9.73	4.73	1.16	0.47	5.59	8.83	302	1014	–0.57	0.91
0110+495	0.788	3.27	4.25	3.84	0.95	0.51	1.88	8.70	4.81	7.44	1.82	0.95	0.39	2.57	3.96	561	891	–0.10	1.25
0212+735	4.291	1.43	1.54	0.58	0.34	0.21	7.52	23.81	4.83	8.51	0.07	0.34	–0.20	4.42	11.91	1230	2066	–0.27	0.91
0219+428	5.810	0.47	0.40	0.25	–0.04	0.23	36.86	19.41	1.23	1.32	0.03	–0.04	–0.11	14.73	18.73	629	923	–0.11	1.15
0248+430	3.329	0.36	0.29	0.13	–0.27	0.10	16.89	33.10	0.51	0.43	0.02	–0.27	–0.03	12.06	32.77	134	1280	–1.02	0.91
0251+393	1.089	0.50	0.43	0.37	0.05	0.31	2.44	78.73	0.81	0.76	0.08	0.05	0.13	1.76	68.95	309	494	–0.12	1.21
0454+844	0.768	0.59	0.52	0.39	0.03	0.23	1.64	–87.66	0.85	0.82	0.11	0.03	0.09	1.36	78.21	229	1030	–0.79	0.74
0537+531	5.592	0.86	0.83	0.31	0.06	0.12	19.15	19.83	2.40	3.20	0.04	0.06	–0.24	7.93	17.25	478	747	–0.14	1.12
0546+726	0.860	0.25	0.18	0.09	–0.42	0.09	3.59	–83.46	0.96	0.95	0.01	–0.42	–0.41	1.38	68.72	99	262	–0.61	0.65
0600+442	5.562	0.07	0.04	0.02	–1.02	–0.05	225.93	20.38	0.63	0.50	0.00	–1.02	–0.87	25.85	20.14	150	461	–0.67	0.65
0609+607	5.657	1.43	1.55	0.45	0.23	0.10	12.25	18.90	4.26	6.90	0.05	0.23	–0.27	6.00	12.97	236	849	–1.65	0.08
0620+389	1.201	1.18	1.22	0.52	0.27	0.21	1.62	52.60	6.63	14.84	0.04	0.27	–0.36	3.50	3.09	351	574	–0.36	0.71
0633+734	16.892	1.41	1.52	0.57	0.30	0.17	102.34	6.73	8.10	19.48	0.05	0.30	–0.40	21.72	5.51	390	732	–0.28	0.98
0710+439	0.894	0.17	0.12	0.05	–0.65	–0.01	5.30	–84.54	0.61	0.51	0.00	–0.65	–0.48	1.79	84.65	161	1505	–1.00	0.92
0731+479	2.005	2.48	3.03	2.50	0.80	0.47	2.25	23.67	4.34	6.73	0.81	0.80	0.29	2.75	10.42	244	511	–0.34	0.96
0733+597	0.212	0.00	0.00	0.00	–2.74	–0.48	249.19	–23.94	0.02	0.00	0.00	–2.74	–1.43	27.26	–23.95	23	132	–1.19	0.37
0743+744	9.740	0.85	0.82	0.28	0.03	0.08	56.72	11.64	1.60	1.84	0.04	0.03	–0.14	30.69	11.42	307	473	–0.19	0.99
0805+410	3.987	1.36	1.45	0.54	0.29	0.18	6.91	25.48	1.61	1.80	0.16	0.29	0.12	6.06	24.53	902	1050	0.08	1.41
0806+573	1.848	0.17	0.11	0.06	–0.61	0.05	13.20	56.53	0.50	0.40	0.00	–0.61	–0.37	4.66	54.20	315	400	–0.11	0.99
0814+425	1.617	2.29	2.76	1.47	0.59	0.29	1.93	25.22	4.27	6.55	0.47	0.59	0.08	2.56	9.25	630	1699	–0.48	0.90
0820+560	2.151	1.87	2.14	0.84	0.45	0.22	2.44	31.18	5.55	10.02	0.13	0.45	–0.14	3.28	7.12	1056	1585	–0.06	1.32
0821+621	1.795	0.10	0.06	0.02	–0.94	–0.08	21.84	58.14	0.32	0.21	0.00	–0.94	–0.55	6.79	57.09	562	583	–0.04	0.95
0831+557	0.396	0.05	0.02	0.01	–1.36	–0.23	12.41	–43.28	0.28	0.17	0.00	–1.36	–0.92	2.23	–45.93	903	4092	–0.81	0.71
0833+416	3.499	1.39	1.49	1.12	0.50	0.38	5.46	27.99	3.69	5.85	0.19	0.50	0.05	3.64	15.71	79	321	–0.69	0.83
0833+585	14.048	0.23	0.17	0.04	–0.66	–0.12		8.14	0.61	0.53	0.00	–0.66	–0.49	161.71	8.13	441	642	–0.18	0.96
0836+710	4.108	3.95	5.35	3.98	1.05	0.54	4.24	14.64	20.76	88.12	0.57	1.05	0.05	10.81	1.05	489	2408	–0.69	0.99
0850+581	1.353	2.86	3.61	1.53	0.66	0.28	1.93	16.70	10.22	24.11	0.26	0.66	–0.13	5.25	1.47	481	1023	–0.39	0.86
0859+470	1.791	2.04	2.39	1.08	0.53	0.27	2.05	29.38	16.52	63.34	0.11	0.53	–0.39	8.39	0.75	435	1151	–0.47	0.90
0859+681	4.550	1.60	1.78	0.76	0.39	0.21	7.57	22.23	3.12	4.36	0.15	0.39	–0.01	5.04	17.19	373	673	–0.30	0.90
0902+490	1.168	1.38	1.49	0.46	0.24	0.12	1.55	45.74	5.23	9.52	0.05	0.24	–0.32	2.84	4.82	476	620	–0.06	1.13
0917+449	2.098	2.00	2.33	1.02	0.53	0.28	2.35	29.56	3.60	5.21	0.22	0.53	0.08	2.55	14.40	777	1407	–0.12	1.36
0917+624	0.547	3.26	4.24	1.33	0.63	0.20	1.83	6.30	8.30	16.35	0.28	0.63	–0.11	4.23	0.92	822	1302	–0.21	0.98
0923+392	2.506	3.41	4.48	1.46	0.69	0.24	2.77	16.50	3.22	4.14	0.91	0.69	0.26	2.74	17.79	9990	7041	0.13	0.94
0954+658	0.159	0.93	0.91	0.55	0.22	0.25	1.02	–70.81	1.04	1.04	0.21	0.22	0.21	1.01	72.88	405	632	–0.54	0.45
1003+830	0.120	3.21	4.16	3.19	0.87	0.44	1.76	1.48	9.51	21.77	0.83	0.87	0.10	4.81	0.15	191	479	–0.57	0.67
1010+350	10.444	3.28	4.26	1.60	0.68	0.24	18.44	9.97	5.59	9.04	0.47	0.68	0.07	12.65	8.53	235	354	–0.41	0.59
1014+615	1.984	1.40	1.50	0.34	0.14	0.01	2.47	39.09	2.02	2.41	0.07	0.14	–0.12	2.23	29.55	466	589	–0.13	0.93
1015+359	6.543	2.56	3.16	1.39	0.62	0.28	9.83	15.14	15.21	49.82	0.18	0.62	–0.28	9.05	2.74	487	701	–0.08	1.19
1020+400	13.107	1.19	1.24	0.46	0.22	0.16	72.92	8.65	7.05	16.06	0.04	0.22	–0.43	15.78	6.78	713	872	–0.04	1.11
1030+611	0.564	1.89	2.18	1.32	0.52	0.29	1.29	21.25	7.72	17.22	0.23	0.52	–0.17	3.95	1.10	236	378	–0.39	0.65
1039+811	10.125	1.89	2.17	1.18	0.56	0.33	28.39	10.91	2.65	3.43	0.37	0.56	0.21	20.84	10.57	825	1214	–0.14	1.06
1041+536	2.506	0.20	0.14	0.05	–0.63	–0.04	18.33	43.29	0.74	0.67	0.00	–0.63	–0.53	5.28	40.68	191	400	–0.40	0.83
1058+629	4.263	0.27	0.20	0.09	–0.42	0.06	35.82	26.31	0.59	0.51	0.01	–0.42	–0.24	16.46	25.94	233	306	–0.48	0.44
1101+384	0.187	0.92	0.90	3.70	0.81	0.84	1.02	–72.80	1.56	1.83	1.12	0.81	0.66	1.11	14.27	370	582	–0.29	0.81
1124+455	2.675	0.82	0.79	0.43	0.17	0.24	5.37	38.07	3.64	6.13	0.04	0.17	–0.27	2.94	15.43	139	359	–0.41	1.01
1144+352	1.886	0.15	0.10	0.05	–0.76	–0.05	15.66	55.65	0.47	0.36	0.00	–0.76	–0.50	5.09	53.64	250	558	–0.42	0.84
1150+812	14.008	1.30	1.38	0.43	0.20	0.11	76.49	8.10	4.63	7.98	0.05	0.20	–0.32	23.60	7.37	637	1233	–0.27	1.04
1240+381	6.421	0.36	0.28	0.06	–0.54	–0.16	59.49	17.65	0.43	0.35	0.01	–0.54	–0.23	49.84	17.63	332	526	–0.36	0.69
1258+507	2.227	1.36	1.45	0.60	0.29	0.18	2.87	37.50	6.33	13.13	0.07	0.29	–0.33	3.64	5.78	193	345	–0.31	0.88
1305+804	3.697	0.03	0.02	0.01	–1.43	–0.18	223.38	30.27	0.35	0.21	0.00	–1.43	–1.09	21.09	30.03	75	146	–0.70	0.39
1307+562	4.648	1.31	1.39	0.73	0.37	0.27	9.28	22.61	2.16	2.69	0.16	0.37	0.10	6.31	20.19	219	323	–0.28	0.78
1309+555	2.986	1.29	1.36	0.58	0.27	0.18	4.50	31.97	1.10	1.12	0.30	0.27	0.24	5.05	33.19	236	292	–0.46	0.43
1333+459	8.175	0.84	0.81	0.21	–0.05	0.01	40.83	13.81	1.09	1.11	0.04	–0.05	–0.08	31.68	13.71	279	643	–0.33	1.07
1335+552	2.202	1.55	1.71	0.76	0.38	0.22	2.66	35.12	3.50	5.17	0.15	0.38	–0.06	2.58	15.32	144	626	–0.75	0.77
1415+463	3.579	0.19	0.13	0.04	–0.67	–0.06	36.44	31.14	0.71	0.63	0.00	–0.67	–0.56	10.11	30.18	157	664	–0.76	0.73
1418+546	2.044	0.97	0.96	0.70	0.27	0.29	3.16	44.82	2.11	2.67	0.15	0.27	0.01	2.28	28.22	1192	2198	–0.16	1.29
1435+638	2.632	0.38	0.31	0.11	–0.30	0.06	10.65	40.93	3.60	6.64	0.01	–0.30	–0.72	2.90	15.55	137	992	–0.76	1.25
1505+428	7.899	0.41	0.33	0.13	–0.30	0.04	78.30	14.39	1.34	1.49	0.01	–0.30	–0.40	24.29	14.04	321	452	–0.10	1.12
1543+517	1.793	0.78	0.73	0.24	–0.01	0.08	3.10	51.84	1.89	2.31	0.03	–0.01	–0.24	2.06	31.76	271	622	–0.30	1.14
1547+507	0.610	4.00	5.44	2.34	0.84	0.33	2.17	4.54	9.30	18.99	0.54	0.84	0.06	4.72	0.81	441	846	–0.21	1.17
1619+491	5.633	1.29	1.37	0.63	0.32	0.22	13.33	19.18	3.41	5.13	0.10	0.32	–0.11	6.50	14.89	204	407	–0.36	0.87
1623+578	10.709	0.53	0.46	0.14	–0.25	–0.01	110.30	10.64	1.25	1.34	0.02	–0.25	–0.33	46.91	10.53	647	777	0.04	1.32
1624+416	8.249	0.54	0.47	0.12	–0.29	–0.07	64.24	13.77	2.66	3.83	0.01	–0.29	–0.63	14.33	12.55	242	1117	–0.75	0.82
1633+382	5.108	3.84	5.19	1.52	0.69	0.19	5.45	14.37	5.62	8.81	0.49	0.69	0.07	5.22	10.23	734	1710	–0.64	0.54
1637+574	5.639	2.40	2.92	1.75	0.70	0.38	8.03	17.14	3.71	5.32	0.60	0.70	0.23	6.28	14.21	696	1830	–0.41	1.01
1652+398	0.221	1.14	1.17	3.28	0.77	0.72	1.03	52.63	2.03	2.58	1.05	0.77	0.53	1.27	7.96	142	888	–0.98	0.65
1700+685	1.037	0.37	0.29	0.15	–0.29	0.08	3.00	84.19	0.62	0.55	0.03	–0.29	–0.12	1.98	77.41	161	227	–0.43	0.52
1716+686	0.505	2.11	2.48	2.52	0.78	0.50	1.35	15.32	2.17	2.59	1.74	0.78	0.49	1.38	14.23	399	750	–0.39	0.76
1726+455	5.686	1.66	1.85	0.61	0.32	0.13	10.89	18.46	1.67	1.88	0.26	0.32	0.13	10.80	18.43	1132	1314	0.03	1.23
1738+476	3.756	1.45	1.57	0.58	0.29	0.16	5.94	26.30	4.47	7.48	0.09	0.29	–0.23	3.93	12.78	514	1080	–0.19	1.37

Table 4. continued.

		$\alpha = -0.75$							observed α										
Source	$\beta_{\rm app}$	$\delta_{\rm IC}$	$\delta_{\rm IC}^{\rm con}$	$\delta_{\rm EQ}$	log $(T_{\rm B}/10^{11})$	log $(T_{\rm Bi}^{\rm con}/10^{11})$	$\Gamma_{\rm sl}$	ϕ	$\delta_{\rm IC}$	$\delta_{\rm IC}^{\rm con}$	$\delta_{\rm EQ}$	log $(T_{\rm B}/10^{11})$	log $(T_{\rm Bi}^{\rm con}/10^{11})$	$\Gamma_{\rm sl}$	ϕ	VLBI flux	VLBI core flux	log $(R_{\rm C})$	$R_{\rm V}$
	[c]				[K]	[K]		[deg]				[K]	[K]		[deg]	[mJy]	[mJy]		
(1)	(2)	(3)	(4)	(5)	(6)	(7)	(8)	(9)	(10)	(11)	(12)	(13)	(14)	(15)	(16)	(17)	(18)	(19)	(20)
1738+499	3.069	1.77	2.01	0.87	0.44	0.23	3.83	27.99	6.28	12.33	0.12	0.44	–0.19	3.97	7.30	270	464	–0.25	0.97
1744+557	0.046	0.31	0.24	0.22	–0.26	0.17	1.78	–5.82	1.12	1.18	0.03	–0.26	–0.30	1.01	19.06	162	356	–0.57	0.59
1755+578	3.950	0.09	0.06	0.02	–1.02	–0.15	87.75	28.40	0.85	0.79	0.00	–1.02	–0.96	10.22	27.28	8	480	–1.75	1.05
1803+784	8.047	2.55	3.13	1.43	0.64	0.30	14.19	12.91	4.36	6.62	0.44	0.64	0.12	9.72	11.01	204	2853	–1.11	1.08
1809+568	1.939	0.29	0.22	0.07	–0.51	–0.06	8.27	53.73	0.90	0.86	0.00	–0.51	–0.48	3.10	47.42	88	475	–0.82	0.82
1823+568	4.497	0.78	0.74	0.42	0.15	0.24	13.91	24.39	3.06	4.71	0.05	0.15	–0.22	5.00	17.48	1414	1278	0.10	1.13
1849+670	8.650	2.39	2.90	1.47	0.63	0.31	17.05	12.27	5.35	9.10	0.36	0.63	0.04	9.76	9.59	391	667	–0.40	0.67
1856+737	0.695	0.84	0.81	0.57	0.24	0.30	1.30	82.00	2.11	2.71	0.10	0.24	–0.02	1.41	19.50	178	434	–0.49	0.80
1908+484	4.095	0.21	0.15	0.07	–0.57	0.00	42.65	27.38	1.08	1.11	0.00	–0.57	–0.60	8.80	25.82	71	145	–0.78	0.34
1924+507	4.522	0.55	0.48	0.23	–0.07	0.15	19.67	24.60	5.48	12.80	0.01	–0.07	–0.63	4.70	10.35	271	422	–0.12	1.19
1954+513	13.003	1.64	1.83	1.08	0.52	0.34	52.73	8.66	4.07	6.53	0.20	0.52	0.04	22.93	8.02	615	1071	–0.42	0.67
2017+745	0.963	5.79	8.55	5.42	1.13	0.49	3.06	3.30	12.39	27.95	1.59	1.13	0.25	6.27	0.72	141	312	–0.55	0.62
2116+818	1.947	0.06	0.03	0.04	–0.82	0.20	38.70	54.33	0.21	0.11	0.00	–0.82	–0.29	11.58	53.95	61	143	–0.79	0.38
2214+350	0.152	0.64	0.58	0.25	–0.06	0.10	1.12	–28.02	2.03	2.59	0.03	–0.06	–0.31	1.27	5.54	534	600	0.05	1.26
2253+417	7.415	0.42	0.35	0.17	–0.17	0.14	66.26	15.31	1.67	2.03	0.01	–0.17	–0.35	17.60	14.64	292	1099	–0.58	0.98
2346+385	5.617	0.26	0.20	0.08	–0.44	0.05	61.70	20.15	0.32	0.25	0.01	–0.44	–0.03	50.37	20.13	565	655	–0.05	1.02
2356+385	2.439	1.19	1.23	0.54	0.29	0.23	3.52	37.50	5.90	12.27	0.05	0.29	–0.31	3.54	6.99	207	382	–0.34	0.85
2356+390	2.346	0.71	0.65	0.35	0.08	0.21	4.96	43.17	2.29	3.09	0.04	0.08	–0.20	2.57	25.71	220	314	–0.23	0.85

Table 5. Calculated values for those sources that have not been detected by *ROSAT* and are not shown in the plots of this paper.

	$\alpha = -0.75$					observed α								
Source	$\delta_{\rm IC}$	$\delta_{\rm IC}^{\rm con}$	$\delta_{\rm EQ}$	log $(T_{\rm B}/10^{11})$	log $(T_{\rm Bi}^{\rm con}/10^{11})$	$\delta_{\rm IC}$	$\delta_{\rm IC}^{\rm con}$	$\delta_{\rm EQ}$	log $(T_{\rm B}/10^{11})$	log $(T_{\rm Bi}^{\rm con}/10^{11})$	VLBI flux	VLBI core flux	log $(R_{\rm C})$	$R_{\rm V}$
				[K]	[K]				[K]	[K]	[mJy]	[mJy]		
(1)	(2)	(3)	(4)	(5)	(6)	(7)	(8)	(9)	(10)	(11)	(12)	(13)	(14)	(15)
0003+380	0.21	0.14	0.05	–0.68	–0.10	0.76	0.70	0.00	–0.68	–0.59	335	721	–0.21	1.31
0022+390	1.23	1.29	0.45	0.21	0.14	4.47	7.67	0.05	0.21	–0.30	130	600	–0.71	0.91
0145+386	0.24	0.18	0.03	–0.76	–0.24	0.58	0.49	0.00	–0.76	–0.57	296	458	–0.10	1.24
0151+474	7.91	12.53	5.58	1.13	0.37	13.07	26.80	2.58	1.13	0.21	717	798	0.15	1.58
0205+722	1.89	2.18	1.42	0.59	0.35	9.11	23.38	0.20	0.59	–0.15	109	272	–0.71	0.49
0249+383	0.31	0.24	0.06	–0.53	–0.10	3.72	6.92	0.00	–0.53	–0.96	216	361	–0.32	0.80
0307+380	3.72	4.99	2.01	0.76	0.27	2.17	2.47	3.43	0.76	0.46	516	521	–0.17	0.69
0340+362	0.59	0.52	0.19	–0.11	0.08	1.11	1.15	0.03	–0.11	–0.15	475	559	0.10	1.49
0604+728	0.20	0.14	0.06	–0.58	0.01	1.42	1.66	0.00	–0.58	–0.69	109	427	–0.78	0.65
0615+820	0.34	0.26	0.06	–0.57	–0.17	1.24	1.33	0.00	–0.57	–0.64	709	782	–0.15	0.78
0636+680	1.07	1.09	0.21	–0.04	–0.06	0.77	0.73	0.08	–0.04	0.06	481	482	–0.02	0.97
0650+371	0.97	0.96	0.38	0.14	0.16	1.41	1.54	0.08	0.14	0.02	334	1310	–0.47	1.34
0650+453	0.95	0.94	0.33	0.07	0.09	5.36	10.62	0.03	0.07	–0.49	415	467	–0.01	1.11
0707+476			0.49	0.23				0.06	0.23		272	854	–0.52	0.94
0730+504	4.83	6.85	3.81	0.97	0.39	5.16	7.53	2.67	0.97	0.37	561	828	–0.20	0.93
0738+491	4.31	5.97	2.18	0.81	0.27	3.31	4.18	1.73	0.81	0.36	677	691	0.28	1.96
0749+426	0.78	0.74	0.19	–0.10	–0.01	6.05	13.14	0.01	–0.10	–0.70	274	424	–0.23	0.92
0803+452	3.46	4.56	2.84	0.88	0.42	7.55	14.48	0.69	0.88	0.17	87	384	–0.68	0.93
0824+355	1.09	1.11	0.16	–0.16	–0.19	5.59	10.42	0.01	–0.16	–0.75	453	659	–0.22	0.88
0929+533	1.04	1.05	0.46	0.16	0.15	5.42	10.77	0.05	0.16	–0.40	133	270	–0.46	0.70
1053+704	3.20	4.14	1.40	0.64	0.21	7.70	14.68	0.27	0.64	–0.08	363	575	–0.27	0.85
1144+402	3.86	5.22	2.13	0.79	0.29	14.63	40.11	0.40	0.79	–0.13	507	639	–0.16	0.86
1218+444	1.65	1.85	0.64	0.32	0.13	7.31	15.57	0.08	0.32	–0.36	390	541	–0.09	1.13
1239+376	0.34	0.27	0.04	–0.70	–0.30	2.07	2.71	0.00	–0.70	–0.95	166	420	–0.43	0.94
1342+663	1.35	1.44	0.29	0.06	–0.05	17.39	67.30	0.02	0.06	–0.88	688	698	0.13	1.37
1355+441	0.03	0.02	0.00	–1.71	–0.44	0.36	0.23	0.00	–1.71	–1.36	195	537	–0.38	1.16
1421+482	0.35	0.28	0.07	–0.51	–0.13	0.63	0.56	0.01	–0.51	–0.35	235	398	–0.36	0.74
1432+422	1.63	1.81	0.62	0.30	0.12	3.30	4.70	0.12	0.30	–0.12	242	298	–0.16	0.84
1534+501	0.15	0.10	0.02	–0.96	–0.27	0.26	0.19	0.00	–0.96	–0.49	180	315	–0.30	0.88
1645+635	2.33	2.81	0.68	0.37	0.06	4.05	5.95	0.14	0.37	–0.13	128	178	–0.54	0.40
1818+356	0.01	0.00	0.00	–2.46	–0.55	0.09	0.03	0.00	–2.46	–1.67	70	70	–0.91	0.12
1839+389	2.56	3.16	1.12	0.55	0.21	4.59	7.08	0.24	0.55	0.01	219	202	–0.34	0.42
1851+488	1.05	1.07	0.31	0.05	0.03	2.41	3.15	0.05	0.05	–0.26	276	273	–0.10	0.78
1936+714	0.90	0.88	0.20	–0.09	–0.06	8.58	22.22	0.01	–0.09	–0.81	227	422	–0.24	1.08
1946+708	0.01	0.00	0.00	–2.20	–0.49	0.08	0.03	0.00	–2.20	–1.36	107	629	–0.78	0.97
2054+611	1.08	1.10	0.55	0.25	0.22	2.95	4.24	0.08	0.25	–0.13	182	360	–0.36	0.87
2229+695	0.52	0.45	0.12	–0.29	–0.04	0.48	0.41	0.03	–0.29	–0.02	273	983	–0.70	0.72
2238+410	1.21	1.26	0.62	0.29	0.22	2.59	3.48	0.12	0.29	–0.05	272	293	–0.40	0.43
2259+371	1.07	1.09	0.34	0.11	0.08	6.88	15.45	0.03	0.11	–0.54	95	341	–0.63	0.84
2309+454	1.31	1.39	0.42	0.18	0.08	1.66	1.88	0.11	0.18	–0.01	375	503	–0.20	0.84
2353+816	2.02	2.36	0.94	0.47	0.21	4.45	7.06	0.19	0.47	–0.05	318	484	–0.17	1.02

Table 6. Calculated values for those sources that have been detected by *ROSAT* but are not shown in the plots of this paper.

	$\alpha = -0.75$					observed α								
Source	δ_{IC}	δ_{IC}^{con}	δ_{EQ}	log ($T_B/10^{11}$) [K]	log ($T_{Bi}^{con}/10^{11}$) [K]	δ_{IC}	δ_{IC}^{con}	δ_{EQ}	log ($T_B/10^{11}$) [K]	log ($T_{Bi}^{con}/10^{11}$) [K]	VLBI flux [mJy]	VLBI core flux [mJy]	log (R_C)	R_V
(1)	(2)	(3)	(4)	(5)	(6)	(7)	(8)	(9)	(10)	(11)	(12)	(13)	(14)	(15)
0010+405	0.55	0.48	0.29	–0.03	0.19	4.12	8.02	0.02	–0.03	–0.49	346	481	–0.48	0.46
0035+367	0.18	0.12	0.06	–0.61	0.03	1.82	2.44	0.00	–0.61	–0.81	91	113	–0.72	0.23
0109+351	3.55	4.70	3.66	0.94	0.47	8.00	15.97	1.16	0.94	0.21	261	379	–0.14	1.05
0153+744	0.07	0.04	0.01	–1.17	–0.21	0.45	0.33	0.00	–1.17	–0.90	87	1264	–1.25	0.82
0309+411	0.17	0.11	0.09	–0.48	0.17	0.37	0.27	0.01	–0.48	–0.14	334	462	–0.19	0.90
0316+413	0.15	0.10	0.15	–0.36	0.34	0.17	0.11	0.04	–0.36	0.28	3080	22410	–1.14	0.53
0402+379	0.02	0.01	0.01	–1.38	0.03	0.13	0.05	0.00	–1.38	–0.70	18	706	–1.72	0.75
0602+673	1.59	1.76	0.62	0.35	0.18	1.79	2.05	0.20	0.35	0.14	244	678	–0.43	1.03
0727+409	2.65	3.30	2.33	0.80	0.44	5.22	8.74	0.54	0.80	0.22	135	417	–0.54	0.89
0746+483	0.54	0.47	0.13	–0.24	–0.01	1.10	1.14	0.01	–0.24	–0.27	472	841	–0.26	0.98
0804+499	1.67	1.87	0.72	0.39	0.20	2.99	4.09	0.16	0.39	0.00	511	1494	–0.38	1.22
0812+367	1.40	1.50	0.44	0.20	0.08	4.54	7.62	0.06	0.20	–0.32	671	950	–0.17	0.97
0821+394	1.86	2.14	1.03	0.53	0.30	7.99	18.34	0.14	0.53	–0.18	673	1063	–0.18	1.05
0847+379	0.60	0.54	0.28	–0.04	0.15	4.13	7.77	0.02	–0.04	–0.51	190	245	–0.30	0.64
0945+408	1.71	1.93	0.59	0.32	0.12	4.52	7.35	0.10	0.32	–0.20	1439	1109	–0.04	0.70
0954+556	0.00	0.00	0.00	–3.33	–0.81	0.01	0.00	0.00	–3.33	–1.74	584	1394	–0.59	0.61
0955+476	4.05	5.53	1.93	0.78	0.27	8.38	15.92	0.48	0.78	0.03	1022	1073	0.09	1.29
1038+528	0.19	0.13	0.04	–0.67	–0.07	0.59	0.49	0.00	–0.67	–0.49	627	749	–0.05	1.06
1044+719	2.10	2.47	0.69	0.38	0.11	1.56	1.70	0.44	0.38	0.22	577	972	–0.62	0.40
1053+815	0.62	0.56	0.25	–0.05	0.12	4.16	7.77	0.02	–0.05	–0.53	522	564	–0.17	0.73
1058+726	1.25	1.31	0.72	0.37	0.29	6.51	14.59	0.07	0.37	–0.26	75	430	–1.10	0.45
1105+437	2.88	3.65	2.07	0.74	0.35	4.72	7.30	0.67	0.74	0.19	253	312	–0.17	0.83
1125+596	2.04	2.39	1.01	0.50	0.24	4.88	8.11	0.19	0.50	–0.05	332	330	–0.07	0.84
1128+385	17.68	33.48	17.06	1.58	0.52	58.91	276.16	5.69	1.58	0.19	592	1005	–0.10	1.35
1213+350	0.02	0.01	0.00	–1.72	–0.29	0.17	0.08	0.00	–1.72	–1.12	31	1002	–1.57	0.87
1226+373	1.39	1.49	0.52	0.26	0.14	0.91	0.90	0.37	0.26	0.30	710	742	–0.13	0.78
1254+571	0.06	0.03	0.01	–1.29	–0.27	0.12	0.06	0.00	–1.29	–0.52	187	188	–0.35	0.45
1300+580	0.61	0.54	0.16	–0.17	0.01	0.62	0.55	0.04	–0.17	0.00	888	903	0.07	1.19
1306+360	6.99	10.77	5.82	1.15	0.43	8.34	13.98	3.79	1.15	0.38	378	418	–0.06	0.96
1347+539	0.29	0.22	0.08	–0.46	–0.01	3.32	5.95	0.00	–0.46	–0.85	427	784	–0.17	1.24
1413+373	0.83	0.80	0.35	0.09	0.15	2.14	2.74	0.04	0.09	–0.18	104	390	–0.57	1.02
1417+385	3.45	4.54	1.21	0.62	0.16	7.44	13.58	0.27	0.62	–0.09	621	619	–0.15	0.71
1427+543	1.95	2.26	0.73	0.40	0.16	8.44	18.99	0.08	0.40	–0.32	317	489	–0.35	0.68
1442+637	1.83	2.09	0.92	0.46	0.24	10.27	27.70	0.11	0.46	–0.32	301	502	–0.18	1.10
1526+670	1.41	1.52	0.46	0.22	0.10	4.32	7.09	0.05	0.22	–0.28	261	414	–0.20	0.99
1531+722	0.27	0.20	0.06	–0.55	–0.07	1.88	2.45	0.00	–0.55	–0.76	170	352	–0.42	0.78
1550+582	2.20	2.62	1.82	0.69	0.40	3.06	4.11	0.64	0.69	0.29	215	287	–0.23	0.78
1622+665	2.45	2.99	2.29	0.72	0.39	2.45	2.98	1.70	0.72	0.39	197	242	–0.42	0.47
1629+495	2.10	2.47	1.72	0.64	0.37	3.92	5.92	0.51	0.64	0.16	322	447	–0.09	1.14
1636+473	2.37	2.88	1.32	0.59	0.27	4.04	6.00	0.40	0.59	0.09	340	750	–0.59	0.56
1638+398	1.94	2.25	0.47	0.25	0.01	2.49	3.12	0.13	0.25	–0.08	1766	1787	0.14	1.39
1638+540	0.18	0.12	0.02	–1.01	–0.38	0.51	0.41	0.00	–1.01	–0.77	205	286	–0.26	0.78
1641+399	2.79	3.50	1.64	0.70	0.33	6.50	11.90	0.41	0.70	0.05	3420	7400	–0.39	0.89
1642+690	0.64	0.58	0.22	–0.07	0.09	1.83	2.24	0.03	–0.07	–0.28	371	1870	–0.61	1.23
1645+410	1.46	1.59	0.70	0.34	0.20	2.96	4.10	0.15	0.34	–0.04	492	570	0.10	1.47
1656+477	1.46	1.59	0.70	0.36	0.22	1.93	2.28	0.20	0.36	0.12	729	1554	–0.29	1.09
1656+571	1.07	1.08	0.54	0.25	0.23	2.60	3.56	0.08	0.25	–0.08	279	417	–0.48	0.49
1719+357	0.87	0.85	0.83	0.33	0.38	1.88	2.31	0.18	0.33	0.11	212	454	–0.61	0.52
1722+401	0.96	0.95	0.48	0.20	0.22	2.65	3.68	0.07	0.20	–0.14	220	391	–0.38	0.73
1739+522	0.92	0.90	0.34	0.11	0.14	8.29	22.67	0.02	0.11	–0.59	1075	965	–0.02	0.85
1745+624	4.29	5.94	2.48	0.87	0.33	17.65	54.24	0.35	0.87	–0.11	329	472	–0.25	0.81
1749+701	0.19	0.14	0.06	–0.60	0.00	2.00	2.80	0.00	–0.60	–0.82	246	1268	–0.47	1.74
1751+441	0.33	0.26	0.09	–0.40	0.01	0.67	0.60	0.01	–0.40	–0.26	717	953	–0.14	0.95
1758+388	2.50	3.06	1.26	0.62	0.28	4.20	6.28	0.31	0.62	0.11	625	919	–0.06	1.27
1800+440	2.25	2.69	1.53	0.64	0.34	4.00	5.99	0.45	0.64	0.15	387	557	–0.47	0.48
1807+698	1.12	1.15	1.11	0.40	0.36	2.72	3.81	0.26	0.40	0.06	579	1604	–0.58	0.73
1834+612	1.64	1.83	0.71	0.37	0.19	3.09	4.28	0.14	0.37	–0.03	368	551	–0.20	0.93
1842+681	4.41	6.14	4.73	1.04	0.49	6.29	10.35	2.49	1.04	0.38	401	851	–0.37	0.91
1928+738	0.31	0.24	0.12	–0.31	0.12	0.96	0.94	0.01	–0.31	–0.30	1383	2835	–0.41	0.80
1950+573	0.52	0.45	0.25	–0.07	0.17	1.82	2.27	0.03	–0.07	–0.27	205	323	–0.37	0.68
2005+642	0.58	0.52	0.13	–0.24	–0.04	0.40	0.34	0.05	–0.24	0.10	805	802	0.04	1.08
2007+777	4.10	5.62	4.24	0.98	0.46	4.23	5.87	3.49	0.98	0.45	1234	2100	–0.02	1.64
2200+420	0.13	0.08	0.15	–0.40	0.35	0.38	0.26	0.01	–0.40	–0.08	838	1988	–0.63	0.55